Acoustic levitation for the study of soft matter on a self-standing droplet

SMARAGDA-MARIA ARGYRI

Department of Chemistry and Chemical Engineering
Chalmers University of Technology
SE-412 96 Gothenburg
Sweden
Phone: +46 (0)31 772 1000

Cover: Top, three techniques used in this thesis to characterize acoustically levitating droplets. Center, an illustration of a multiple-transducers acoustic levitator with a levitating, self-standing droplet. Bottom, a photograph, an MRI, and a 2D scattering pattern acquired from levitating droplets.

Acoustic levitation for the study of soft matter on a self-standing droplet
SMARAGDA-MARIA ARGYRI
Department of Chemistry and Chemical Engineering
Chalmers University of Technology

Abstract

Contact-free studies allow the investigation of surface and interfacial phenomena without the shortcomings of surface-induced effects. In comparison to other contact-free techniques, an acoustic levitator can trap any low-volume (< 10 mm^3) material in mid-air. Recent developments and findings have advanced the experimental and theoretical understanding of acoustic levitation; however, the levitation stability and capacity are often far from ideal for studying physicochemical properties of liquids. In this thesis, the designing principles of acoustic levitators were explored, allowing the customization of high-performing devices. The surface tension of acoustically levitated droplets of aqueous surfactant solutions was determined through a data-driven approach. The high stability of the developed levitator allowed the training of a deep neural network with over 50,000 high-quality photographs of droplets. The surface tension, predicted by the neural network, presented accuracy equal to or higher than that of theoretical models, which allowed the determination of the critical micelle concentration on a single droplet. Following, a study on surface freezing was conducted on binary hexadecane/water droplets, above the melting temperature of the alkane. The conditions to induce surface crystallization were explored and the solid phase was characterized in a contact-free manner by coupling Raman spectroscopy with an acoustic levitator operating horizontally. The high performance of this family of acoustic levitators also allowed the operation of a demagnetized version in a 7.05 T magnetic field, thereby granting the implementation of magnetic resonance studies on a self-standing droplet. Finally, a pH-responsive system was investigated by levitating microliter droplets and exposing them to CO_2. The occurring phase transition was characterized through optical means, magnetic resonance spectroscopy, and X-ray scattering, free from surface-induced artifacts.

Keywords: Droplet, contact free, surface properties, soft matter, magnetic resonance.

ii

List of Publications

I **Customized and high-performing acoustic levitators for contact-free experiments**
<u>Smaragda-Maria Argyri</u>, Carl Andersson, Nicolas Paillet, Lars Evenäs, Jens Ahrens, Asier Marzo, Victor Contreras, and Romain Bordes
Journal of Science: Advanced materials and devices, 9, 3, (2024), 100720

II **Contact-free measurement of surface tension on single droplet using machine learning and acoustic levitation**
<u>Smaragda-Maria Argyri</u>, Lars Evenäs, and Romain Bordes
Journal of Colloid and Interface Science, 640, (2023), 637-646

III **Crystallization at the hexadecane/water interface observed under acoustic levitation**
<u>Smaragda-Maria Argyri</u>, Axel Stark, Viktor Eriksson, Lars Evenäs, Anna Martinelli, and Romain Bordes
Manuscript

IV **Contact-free magnetic resonance imaging and spectroscopy with acoustic levitation**
<u>Smaragda-Maria Argyri</u>, Leo Svenningsson, Feryal Guerroudj, Diana Bernin, Lars Evenäs, and Romain Bordes
Submitted

V **Combining X-ray scattering and magnetic resonance with acoustic levitation to investigate CO_2 induced phase transitions on a self-standing droplet**
<u>Smaragda-Maria Argyri</u>, Maëva Almeida, Fabrice Cousin, Diana Bernin, Lars Evenäs, Anne-Laure Fameau, Clemence Le Coeur, and Romain Bordes
Manuscript

My Contributions to the Publications

Paper I
Main author. Performed all experimental work and wrote the Python code, except the code for simulations, frequency response plots, and Docker images for the online framework.

Paper II
Main author. Performed all experimental work, except the design and construction of the acoustic levitator. Built and evaluated the machine learning algorithm.

Paper III
Main author. Planned and supervised the experimental work. Performed additional experiments on the effect of humidity and added surfactants on the system.

Paper IV
Main author. Performed the majority of the experimental work, data analysis, and processing. Did not develop the theoretical part.

Paper V
Main author. Took part in the experimental planning, and performed the majority of the acoustic levitation experiments. Implemented the data analysis for all the measurements except for the scattering experiments.

List of Abbreviations and Acronyms

CMC: Critical micelle concentration

CTAB: Cetyltrimethylammonium bromide

DNN: Deep neural network

DSC: Differential scanning calorimetry

FISP: Fast imaging with steady-state free precession

FLASH: Fast low angle shot

fps: Frame(s) per second

HSA: Hydroxysteric acid

ISIS: Image-selected *in vivo* spectroscopy

MAE: Mean absolute error

MEA: Monoethanolamine

ML: Machine learning

MR: Magnetic resonance

MRI: Magnetic resonance imaging

MRS: Magnetic resonance spectroscopy

MSE: Mean squared error

NA: Numerical aperture

NMR:	Nuclear magnetic resonance
NN:	Neural network
PLA:	Polylactic acid
PRESS:	Roint resolved spectroscopy
pxl:	Pixel(s)
RARE:	Rapid acquisition with relaxation enhancement
RF:	Radiofrequency
SANS:	Small-angle neutron scattering
SAXS:	Small-angle X-ray scattering
SDS:	Sodium dodecylsulfate
SPL:	Sound pressure level
STEAM:	Stimulated echo acquisition mode
TEG:	Triethylene glycol
WAXS:	Wide-angle X-ray scattering

Contents

<div style="text-align: right; font-size: 4em; color: #999;">1</div>

Introduction

The behavior of molecules at interfaces often differs significantly from the behavior in the bulk phase. Surface chemistry comprises the scientific field that delves into the molecular interactions, occurring at the interface between bulk matter and its surroundings. These interactions are present in everyday life; from cleaning our hands to self-cleaning surfaces to catalysts to non-stick cookware, and so on. Yet, the study of interfaces often remains challenging, due to the presence of surface boundaries.

Many techniques allowing contact-free studies have been developed. Optical tweezers[1–3], magnetic levitation[4–6], electrostatic levitation[7–9], and others[10–14] are well documented. Through these techniques, small-volume samples (typically around 0.1-10 µL), can be captured and manipulated in real-time, finding applications in biochemical studies[12], where the available volume may be limited (*e.g.*, blood samples from small animals[15]), or in cases where, surface intervention needs to be avoided (*e.g.*, heat transfer[16], omnidirectional evaporation[17], glass formation[18], *etc.*). In comparison to the other techniques, acoustic levitation presents the advantage of levitating any material. The main limitation originates from the magnitude of the generated acoustic forces, leading to a maximum weight that can be kept aloft.

The first acoustic levitator was based on the invention of an ultrasonic probe for submarine detection, developed by Paul Langevin and Constantin Chilowsky[19,20]. Specifically, the ultrasonic probe, later named the Langevin horn, was coupled with a reflector as shown in Figure 1.1a. The interference between the ultrasonic waves

<div style="text-align: right;">1</div>

produced by the probe and the ones reflected yields a stable, airborne acoustic pressure field. As in the case of standing waves, the acoustic pressure field is described by areas of low (*i.e.*, nodes) and high pressure (*i.e.*, anti-nodes) that appear to be immovable in space. The acoustic nodes act as physical traps for objects with a diameter smaller than half a wavelength (approximately 4.28 mm, for an operating frequency of 40 kHz). The acoustic forces below the node counteract gravity, while the presence of lateral forces can influence the spatial stability of the levitated object.
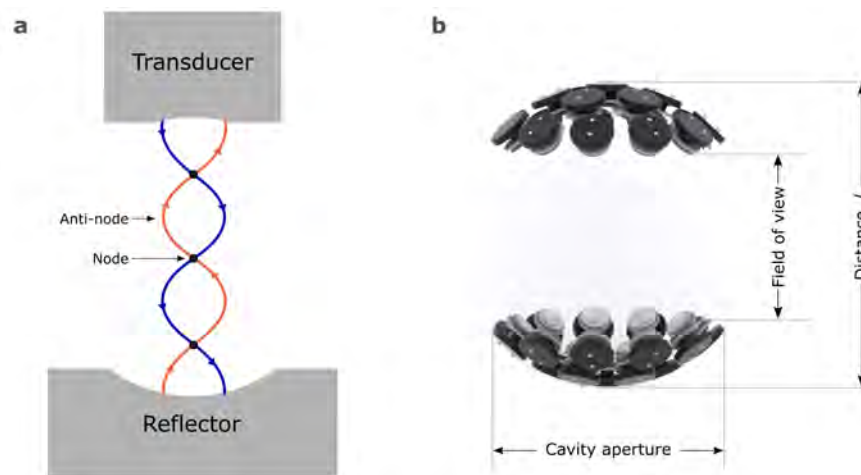
Figure 1.1: (a) Illustration of a Langevin horn and simplified representation of a standing wave being generated when the opposing acoustic waves (blue and orange line with arrows) interact. The acoustic nodes and anti-nodes denote the areas with the lowest and highest time-averaged acoustic pressure, respectively. (b) Photorealistic illustration of a multiple-transducers acoustic levitator. The main design parameters are displayed.

The Langevin horn usually operates at a frequency range of 20-40 kHz and it requires high voltage (> 100 V) to operate since the acoustic pressure field is generated by one emitter[21,22]. Although the device is simple to build, its performance can be highly sensitive to changes in humidity and temperature, thus requiring frequent tuning through manual adjusting of the distance between the emitter (*i.e.*, transducer) and the reflector[22,23]. Additionally, the lateral forces are typically low[24]. Consequently, it can be challenging to position a sample within the acoustic trap, while the lateral spatial stability of the sample may be low during levitation.

Figure 1.2: a) Illustration of an axis-symmetric multiple-transducers acoustic levitator, with distance of opposing arrays, L, b) geometrical parameters that describe the cavity design, where D and a are the diameters and radius of circular aperture, respectively, r is the radius of curvature that defines the radius of the imaginary sphere the transducers are placed on (dashed line) and θ is the opening angle from the center of the imaginary sphere, c) illustration of a spherical arrangement of 36 transducers distributed on three concentric rings, which corresponds to the design of TinyLev[25]. Reproduced with permission from Reference [24].
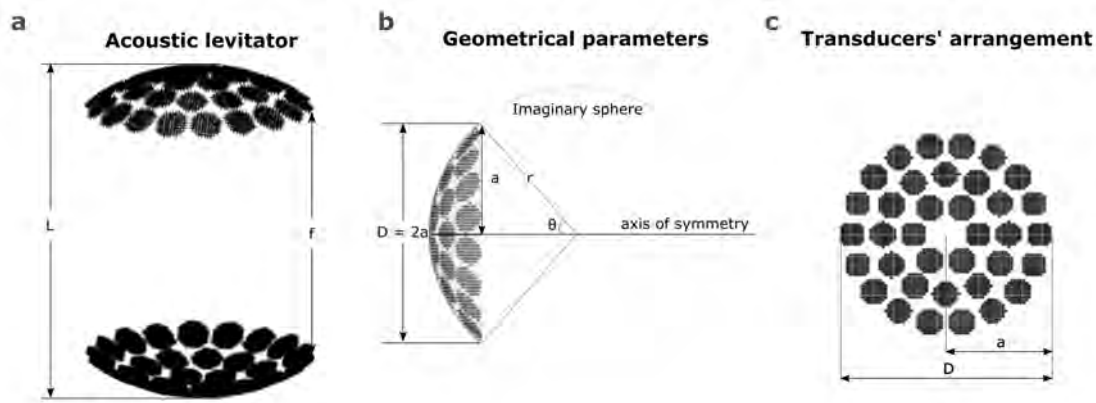
A new generation of acoustic levitators that utilize multiple transducers (Figure 1.1b) has recently gained significant attention due to low cost, low driving voltage (< 20 V), and the possibility to subdivide the arrays into groups with different phases[26]. The control over the acoustic pressure field has allowed rotational[27] and spatial control over the levitated sample[28–31]. Furthermore, the presence of multiple transducers offers design flexibility, which allows the customization of acoustic levitators for different applications.

The performance of the acoustic levitator, in terms of levitation strength and spatial stability of the sample, can be controlled by adjusting the design parameters (Figure 1.2), and the operating parameters (*i.e.*, operational frequency, phase, *etc.*). In a recent study, Marzo *et al.*,[25] reported a concave acoustic levitator with multiple transducers, called TinyLev. According to Adamowski *et al.*,[32] placing the transducers on a concave plane leads to an improved performance as the acoustic force is concentrated locally. The TinyLev levitator consists of 72 transducers in total, which are equally distributed into two concave planes of transducers, with a cavity aperture of 60 mm.

The distance of opposing arrays was 120 mm and the transducers were positioned in a circular arrangement. It was reported that the device could levitate samples with a density of up to 6.5 g/cm^3 and, without being highly influenced by environmental conditions, while in a later study, mercury (13.5 g/cm^3) was levitated by adjusting the spatial arrangement of the transducers[33].

1.1 Purpose and objectives

Despite recent advances in the field[25,33], further improvements related to spatial stability, and levitation capacity of the levitators are required to decrease experimental noise and facilitate the use of acoustic levitation for physicochemical studies. Consequently, two main objectives are defined and covered in this thesis. The first objective was to develop and evaluate the performance of new acoustic levitators (Paper I). The second objective was to illustrate the applicability of these devices in the study of surface and bulk properties of liquids (Paper II to Paper V).

In Paper I, the influence of the designing parameters of acoustic levitators on the acoustic pressure, stability, and levitation capacity was evaluated. Three concave acoustic levitators (Mk1, Mk2, and Mk3) were developed and evaluated through simulations and experimental measurements. Furthermore, an interactive online tool was developed to allow the user to define the desired design parameters and simulate the acoustic pressure field for the specific configuration. A suitable file for 3D printing can be generated, encouraging the customization of acoustic levitators for practical applications.

In Paper II, the surface tension of acoustically levitated droplets was determined through a data-driven approach. A series of droplets of surfactant solutions were levitated and evaporated over a period of 30 min, while the voltage (*i.e.*, the acoustic pressure) was simultaneously varied. More than 50,000 images of the levitated droplets were acquired. Following, the data were fed into a deep neural network (DNN), which uncovered patterns in the data without any set preconditions. This led to determining the surface tension of levitating droplets with a mean absolute error (MAE) of 0.88 mN/m while surpassing previously reported limitations related to the shape and size of the droplets.

In Paper III, a two-droplets system was investigated. Specifically, a droplet of hexadecane and a droplet of water were simultaneously levitated, at constant voltage. Through optical means, the propagation of a macroscopic surface freezing of hexadecane was observed 3 °C above the melting point. After a significant volume of water had evaporated, the droplet of hexadecane returned to the liquid state. The presence of a solid phase was confirmed and characterized through Raman spectroscopy in a contact-free manner, and the melting kinetics were quantified.

In Paper IV, a demagnetized acoustic levitator was developed and operated in a 7.05 T magnet. The performance of the levitator in the presence of the magnetic field was evaluated, and magnetic resonance images and spectra were acquired on self-standing droplets. Furthermore, the relationship between droplet shape and chemical shift was established, as a clear downfield shift was induced when the droplet shape changed from spherical to oblate. Finally, time-resolved experiments on pure solvents and mixtures were conducted, capturing physical and chemical processes in real-time due to evaporation.

In Paper V, a pH-responsive system was evaluated in a contact-free manner by acoustically levitating a droplet and exposing it to CO_2. The structural transition of the self-assemblies was evaluated through optical means, X-ray scattering, and magnetic resonance spectroscopy. This approach allowed the direct study of systems in the microliter regime, without compromising the performance of advanced analytical tools, and provided a suitable background for the investigation of complex systems *in-situ*.

2

Background

2.1 Acoustic pressure field

Acoustic waves bear energy which induces mechanical vibrations as it travels through a medium. When opposing acoustic waves with the same wavelength, λ, interact, they can alter the pressure of the medium locally. Simple sonotrodes, such as Langevin horns, create a stable acoustic pressure field through the interference of the acoustic waves generated by the ultrasonic horn and the opposing acoustic waves reflected by the reflector. When multiple sources are involved, the generated acoustic pressure field can be simulated by summing the individual pressures that each source produces. The radiation pattern of the ultrasonic transducers - also known as directivity - refers to the pattern of the generated sound pressure level (SPL) propagating in space. Based on this pattern, different solutions to the wave equation are found.

Here, we assume that each transducer behaves like a single-point source and that the sound pressure propagates homogeneously around the point source, like a circular ring. In that case, the acoustic pressure, p_j, is expressed as:

$$p_j = \frac{e^{ikr_j}}{r} J_0(kr_j \sin \theta_j) \tag{2.1}$$

where, r is the effective radius of the transducer, r_j is the distance between the transducer j and the levitation point, k is the wavenumber, J_0 is the Bessel function of the first kind of order 0, and θ_j is the angle between the transducer and the z-axis.

2.1.1 Acoustic radiation force on rigid objects

When an object is introduced into the acoustic pressure field, the acoustic waves will be partially scattered on its surface and the object will experience the so-called acoustic radiation force. This force can be described from the scattering theory for rigid objects. Within the linear time-harmonic regime, the mass and momentum conservation equations in the medium are expressed as[34]:

$$\text{div}(\mathbf{v}) = \mathrm{i}\omega p / K \tag{2.2}$$

and,

$$-\mathrm{i}\omega\rho\mathbf{v} = -\nabla(p) \tag{2.3}$$

where, $\text{div}(\mathbf{v})$, is the divergence of the particle velocity, v, p, is the acoustic pressure, K, is the bulk modulus of the medium, which is defined as $K = \gamma P_0$, ρ, with γ being the adiabatic constant and P_0 the atmospheric pressure in ambient conditions, and ω is the angular frequency. $\nabla(p)$ is the gradient of acoustic pressure, which is defined as:

$$-\nabla(p) = \left(\frac{\theta p}{\theta x}, \frac{\theta p}{\theta x}, \frac{\theta p}{\theta x} \right) \tag{2.4}$$

By combining Equations (2.2) and (2.3), we acquire the Helmholtz equation[34]:

$$\Delta(p) = k^2 p = 0 \tag{2.5}$$

where, k is the wavenumber defined as: $k = \omega/c$, and c is the speed of sound in the medium.

To solve the Helmholtz equation and acquire the pressure of the acoustic field around the object, we need to apply the boundary conditions around the surface, Γ_j, of the object. We define the simplest case of a rigid (*i.e.*, non-permeable) object that is not moving in space. This means that the normal component, n_j, of the particle velocity will be zero. In that case, we apply the following boundary condition:

$$\nabla(p) \cdot n_j = 0 \tag{2.6}$$

To determine the normals, n_j, we need to define the shape of the object. In case the object is spherical and small in comparison to the wavelength, the condition $ka \ll 1$ applies (where, k is the wavenumber and a is the radius of the spherical object). In this case, the acoustic radiation force is expressed as:

$$F = -\nabla U \tag{2.7}$$

where, U is the Gor'kov potential:

$$U = 2\pi R^3 \left(\frac{\langle p^2 \rangle}{3\rho c^2} - \frac{\rho \langle u^2 \rangle}{2} \right) \tag{2.8}$$

In the case of an ellipsoidal object, the force applied to the object varies throughout the surface. To solve this case, the spheroidal Bessel functions that describe the surface need to be derived[35]. This case is relevant for liquids that can be deformed towards ellipsoidal shapes.

2.1.2 Acoustic radiation force on permeable objects

In the case of permeable objects, the acoustic waves will be partially absorbed by the object and partially reflected in all directions. The proportion of the acoustic wave intensity reflected on the boundary of the object depends on the difference between the acoustic impedance of the traveling medium (Z_1) and that of the object (Z_2). Where, the acoustic impedance of a material, in the simplest case, is defined as:

$$Z = \rho v \tag{2.9}$$

And, the intensity reflection coefficient, which describes the percentage of acoustic waves reflected is expressed as:

$$a = \left(\frac{Z_2 - Z_1}{Z_1 + Z_2} \right)^2 \tag{2.10}$$

where ρ and v are the density and the speed of the sound in the medium, respectively. For the case where air is the wave propagating medium (Z_1 = 413 kg/(m^{2}s)) and water is the levitating object (Z_2 = 1.48 * 10^6 kg/(m^{2}s), at 20° C), then the intensity reflection coefficient, a is found to be 99.9%. Hence, the majority of the acoustic waves are reflected on the surface of the water droplet due to the large density difference between the media.

For spherical objects, the acoustic pressure field inside the object is expressed as[34]:

$$p_j^{in} = \sum X_n^j \zeta_n^j(r_j) \tag{2.11}$$

where,

$$\zeta_n^j(r_j) = J_n(k_j r_j) e^{in\theta_j} \tag{2.12}$$

where, X_m^j are complex coefficients, $\zeta_n^j(r_j)$ are the cylindrical wavefunctions and $J_n(k_j r_j)$ are the Bessel functions of the first kind.

Ultrasonic transducers allow the acoustic levitation of samples, due to nonlinear effects that result from the high-power acoustic waves involved. Hence, the analysis needs to be performed in the non-linear regime. The medium is governed by the mass, momentum, and energy conservation equations:

Mass conservation:

$$\frac{D\rho}{Dt} + \rho \nabla \cdot v = 0 \tag{2.13}$$

where,

$$\frac{D\rho}{Dt} \equiv \frac{\theta}{\theta t} + v_i \frac{\theta}{\theta x_i} \tag{2.14}$$

Momentum conservation:

$$\rho \left(\frac{\theta v}{\theta t} + (v \cdot \nabla)v \right) = -\nabla p + \eta \Delta v + (\zeta + \frac{\eta}{3} \nabla^2 v) \tag{2.15}$$

Energy conservation:

$$\rho T \left[\frac{\theta s}{\theta t} + (v \cdot \nabla)s \right] = \kappa \Delta T + \zeta (\nabla \cdot v)^2 + \frac{1}{2} \eta (\theta_i v_j + \theta_j v_i) - \frac{2}{3} \nabla \cdot v \delta_{ij})^2 \tag{2.16}$$

where ρ is the density of the medium, v, is the particle velocity, p is the pressure, t is time, x is the space coordinate, η is the dynamic viscosity, ζ is the bulk viscosity, $v = -\nabla \Phi$, with Φ, being the velocity potential, κ is the heat conduction number, δ_{ij} is the Kronecker tensor. For the derivations and more information on nonlinear

acoustics, please refer to Enflo and Hedberg[36]. The theoretical framework presented above has been implemented in the Python library *Levitate*[37] and has been used as a tool for theoretical calculations in this work.

2.1.3 Piezoelectric transducers

The main component of an acoustic levitator is the piezoelectric transducer, which converts the electrical signal to mechanical vibrations and *vice versa*. As a result, a transducer can function both as an emitter and a receiver of acoustic waves. When electric current passes through them, mechanical vibrations are induced, generating acoustic waves in the ultrasonic regime. Conversely, if mechanical force is applied then a charge is produced. The relation between the applied charge, Q, and the force, F, generated is expressed as:

$$F = \frac{Q}{d}$$
(2.17)

where, d is the piezoelectric coefficient.

From Equation (2.17), it is evident that the higher the applied charge (*i.e.*, power), the higher the amplitude of the force. Conversely, the higher the force received, the higher the generated charge will be.

Furthermore, piezoelectric transducers can be modeled as a series L-C circuit, where the electrodes on the piezo plate and the resonating mass act as a capacitor and an inductance, respectively[38]. Hence, the resonant frequency, f_{res}, of the circuit is found when the capacitive reactance, (x_C), and inductive reactance, (x_L), are equal. Where:

$$x_C = \frac{1}{2\pi f C}$$
(2.18)

and,

$$x_L = 2\pi f L \tag{2.19}$$

Solving for Equations (2.18) and (2.19):

$$f_{res} = \frac{1}{2\pi\sqrt{LC}} \tag{2.20}$$

where, C, is the capacitance, and L, is the electrical inductance of the circuit.

When the circuit operates at the resonant frequency, the impedance of the circuit is minimized, while the current consumption is maximized. Hence, the power transferred from the transducers to the medium is maximum. In practice, transducers are not ideal components and the resonance may be affected by the environmental conditions (*e.g.*, temperature, humidity, *etc.*), neighboring transducers, and the voltage applied. For that reason, it is recommended to experimentally determine the resonant frequency of the circuit to ensure optimum operational frequency.

2.2 Surface tension and capillary length

Surface tension is a property of liquids, which arises from the imbalanced cohesive forces experienced by the molecules on the surface of the liquid. The molecules in the bulk experience omnidirectional, cohesive forces due to the neighboring molecules. However, the molecules on the surface experience an inward net force, which aims to minimize the surface energy, by minimizing the surface area of the liquid. The higher the cohesive forces between the molecules, the more energy is required to change the area of the liquid. Hence, in terms of energy, surface tension can be defined as the amount of energy required to increase the surface area by one unit area:

$$\gamma = \frac{W}{\Delta A} \tag{2.21}$$

where, W is the work and ΔA is the surface area difference.

The quantitative and empirical studies performed by Thomas Young, in 1805[39] and the mathematical analysis by Pierre-Simon Laplace, in 1807[40], led to the so-called Young-Laplace equation, which correlates the pressure difference on the boundary between the medium (*e.g.*, air) and the liquid of study (Δp), to the surface tension (γ) and the total surface curvature of a liquid droplet ($\nabla \cdot n$), when in equilibrium:

$$\Delta p = -\gamma \nabla \cdot n \tag{2.22}$$

The pressure difference (ΔP) is also known as the Laplace pressure. For spherical droplets with radius, R, the Laplace pressure is defined as:

$$\Delta P = P_{\text{inside}} - P_{\text{outside}} = \frac{2\gamma}{R} \tag{2.23}$$

Therefore, the shape of a free-standing droplet will be governed by its surface tension which tends to be spherical unless the hydrostatic pressure resulting from the gravitational forces comes into play. Hence, the Laplace pressure increases as the size of the droplet decreases. The radius at which the Laplace pressure equilibrates the hydrostatic pressure is called capillary length, λ_c (Equation (2.24)), and defines a theoretical threshold above which the gravitational forces will have a greater influence on the shape of a droplet:

$$\lambda_c = \sqrt{\frac{\gamma}{\rho\, g}} \tag{2.24}$$

where, ρ is the density and g is the gravity acceleration.

2.2.1 Surfactants

Surfactants are molecules that present surface activity due to the presence of a hydrophilic part and a hydrophobic part. The surface activity of surfactants depends on numerous parameters (*e.g.*, length of hydrophobic part, charge, size of hydrophilic part, *etc.*), while, depending on the charge of the hydrophilic part two main types of surfactants can be defined: ionic and non-ionic. Surfactants tend to accumulate at interfaces between the polar phase (*e.g.*, water) and the non-polar phase (*e.g.*, oil or air), reducing the interfacial tension. When the concentration of surfactants in solution reaches a critical concentration, surfactants begin to self-assemble into spherical micelles, to reduce the free energy of the system. This concentration is called the critical micelle concentration (CMC), and above that value, the surface tension remains constant.

2.2.2 Determination of surface tension through acoustic levitation

The level of acoustic radiation force applied to a levitating droplet influences the shape. As shown in Figure 2.1a-c, the 2D projections of the droplet will vary from circular, indicating a spherical shape, to ellipsoidal, indicating an oblate shape, depending on the volume, voltage (*i.e.*, acoustic pressure), and surface tension of the liquid. In Figure 2.1a, the influence of droplet volume on the shape is shown for droplets that have the same surface tension and experience the same voltage. It is observed that the lower the volume, the more spherical the droplet will be, as the droplet will experience a lower degree of acoustic radiation force on its surface. In Figure 2.1b, it is shown that under constant volume and surface tension, the shape of the droplet is less spherical for higher driving voltage. The driving voltage defines the amplitude of the acoustic pressure generated by the transducers. As a result, the applied acoustic pressure increases, as the driving voltage increases. Lastly, in Figure 2.1c, the effect of surface tension is shown, when the volume and voltage are identical. It is observed that for lower surface tension, the less spherical the droplet will be, due to the lower capacity of the droplet to withstand the applied acoustic pressure.
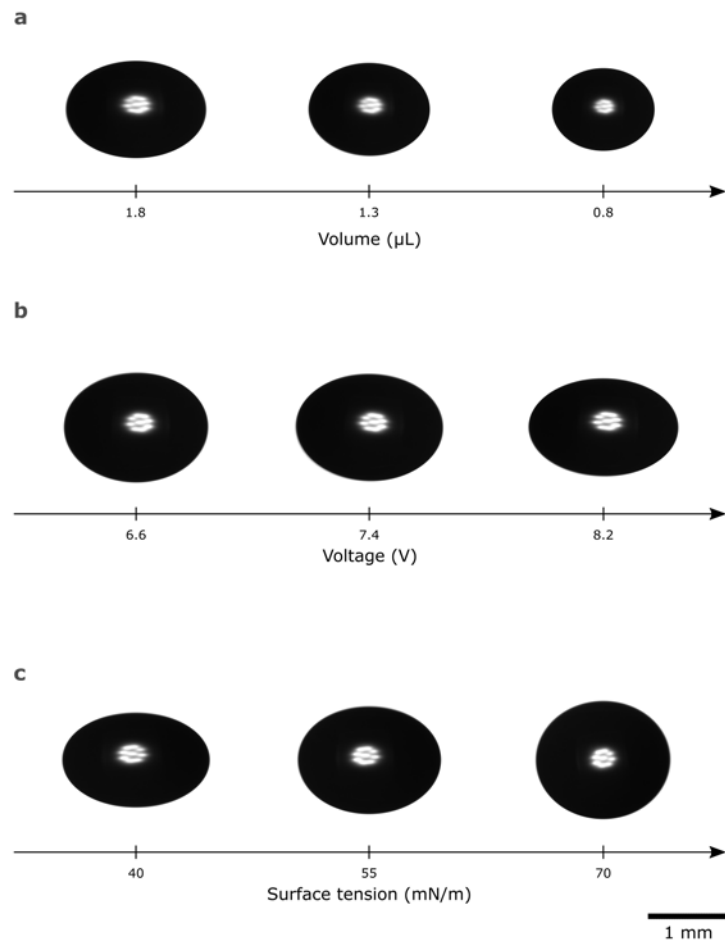
Figure 2.1: Relation between the deformation of an acoustically levitated droplet with the (a) volume, for voltage of 9.0 V and surface tension of 29 mN/m (b) voltage, for volume of 2.1 μL and surface tension of 48 mN/m, and (c) surface tension, for volume of 2.0 μL and voltage of 7.0 V.

The first attempt to develop a theoretical model correlating the shape of an acoustically levitated droplet to the surface tension, γ, was implemented by Trinh and Hsu[41]. The authors studied various substances with constant surface tension, using a Langevin horn. They calculated the acoustic radiation force according to the Gor'kov theory[42] and utilized the equations derived by Marston *et al.*,[43,44] to mathematically describe the equilibrium shapes of the acoustically levitated droplets, as:

$$r(\theta) = R + x(\theta) \tag{2.25}$$

where, R is the equivalent spherical radius of the droplet for a certain volume and $x(\theta)$ describes the deviation from sphericity as:

$$x(\theta) = -\frac{3}{64\gamma}(3\cos^2\theta - 1)R^2 P_s^2 \beta_0 \left(1 + \frac{7}{5}(kR)^2\right) \tag{2.26}$$

where, θ is the azimuth angle, β_0 and k are the compressibility and wavenumber of the host medium (*i.e.*, air), respectively.

Although Equation (2.26) is simple and easy to implement, it employs several simplifications and assumptions, limiting its applicability. Specifically, the Gor'kov theory[42], which is accounted for, in the model, is valid for spherical droplets with a maximum radius that is 1/10 of the operating wavelength of the device (f = 25 kHz, for Langevin horns). Another condition is that the radius must not exceed the capillary length of the liquid, as the gravitational force will be higher than the Laplace pressure. This will cause the droplet to be flattened at the bottom due to its own weight, inducing an asymmetry in shape. Lastly, the acoustic pressure applied on the surface of the droplet needs to be determined. This has traditionally been done with a microphone, yet, non-linear acoustic effects present in the ultrasonic regime may decrease the accuracy of the measured acoustic pressure[45].

Tian *et al.*,[21] developed a more detailed and analytical model. In this publication[21], an optimization algorithm to determine the shape and the position of an acoustically levitated droplet in space was developed. The shape of the droplet was described through a Legendre function. The wave field inside the droplet was derived from a Bessel function after combining Green's function, Helmholtz formula, and the spherical Hankel function of the first kind. The acoustic radiation pressure on the surface of the droplet was determined by accounting for the sound pressure and particle velocity inside and outside of the droplet. Then, through a loss function and multiple iterations, the Legendre constants and the Bessel coefficients were determined by minimizing the difference between the derived sound intensity or aspect ratio and the experimental values measured with a microphone and the camera, respectively.

This algorithm was applied in a following publication by Tian *et al.*,[46] and the surface tension of acoustically levitated samples was determined with an error of ± 2 mN/m when the surface tension was lower than 50 mN/m. The authors stated that the error was high compared to other techniques (typical statistical error: ± 0.5 mN/m) due to the low spatial stability of the acoustic levitator they used.

It should be noted that in both studies mentioned above, a Langevin horn was used. Based on simulations (Supporting Information, Paper I), this acoustic levitator presents a simple acoustic pressure field, with low lateral forces. In contrast, multiple-transducers levitators generate a more complex pressure field. As a result, more complex equations than the ones presented here are required for correlating droplet deformation and surface tension.

2.3 Soft-matter and phase transitions

Materials are made of atoms that are structurally arranged in a way that defines their characteristics. The structural arrangement can be altered by changing conditions, such as temperature, pressure, concentration, or pH, causing a so-called phase transition. A well-known example of phase transition is the ice-water-steam transition, which can be easily accomplished by changing the temperature of the system.

Alkanes are a class of saturated hydrocarbons that exhibit an intriguing property, namely surface freezing. This property was discovered in 1932 by Müller[47] and describes the phenomenon where these molecules align at the liquid/air interface in a hexagonal pattern, forming a crystalline monolayer. This effect occurs up to 3 °C above the melting point and was characterized by X-ray[48] and surface tension[49] measurements, but recently it has mainly been examined through simulations.

Surfactants on the other hand, with concentration above the CMC, can form self-assemblies in the bulk, as mentioned above. The structure of these self-assemblies can be affected by the concentration, temperature, and pH, leading to a change of the molecular organization, *i.e.*, a phase transition. In order to describe the boundaries at which these transitions occur, phase diagrams are made, which describe the conditions under which a phase or a mixture of phases is present.

2.4 Machine learning

Machine learning is a statistical tool that can, without pre-assumptions, uncover patterns in large datasets, surpass heuristic model limitations, and accelerate the solution of computational and analytical challenges[50]. Different types (*i.e.*, supervised, unsupervised, reinforced), and methods (*i.e.*, classification, regression), of machine learning algorithms, have been developed, aiming to tackle different challenges.

In this section, the case of supervised deep neural networks (DNN) for regression analysis will be accounted for. On its whole, supervised machine learning aims to develop a regression function, f that correlates the input data, x, with the predicted output parameter(s), $\hat{y}$, as:

$$\hat{y}(x) := f(x, W) \tag{2.27}$$

For this type of machine learning algorithm, the desired output parameter(s) need to be known, through, for instance, experimental measurements. In machine learning terminology the values used for the training of the neural network (NN) are commonly called *True values*, while the ones the NN outputs after the training are called the *Predictions*. The machine learning algorithm develops and applies statistical approximations with no pre-set assumptions between the input and output, hence empirical and theoretical limitations employed by previous models may be surpassed. During training, the neural network has access to a fraction of the data (*i.e.*, training dataset) which allows the adjustment of the model parameters, also known as weights, W. The choice of these parameters is evaluated on a fraction of the training dataset (*i.e.*, validation dataset) through a loss function. Finally, the evaluation of the trained NN is performed on the remaining data (*i.e.*, test dataset). The most commonly used loss function is the least squared norm of the error between the output values, y and the predicted values $\hat{y}$:

$$L(y, \hat{y}(X)) := ||y - \hat{y}(X)||_2^2 \tag{2.28}$$

The smallest component of a neural network is the neuron (Figure 2.2). Similarly to the biological neurons, these components receive certain inputs and after weighing them, they reach certain outputs. Specifically, after weighing each input, the neuron sums those weights and passes them through an activation function. If a certain threshold is exceeded, the neuron is activated - meaning that the received information was found important. Depending on the activation function, the output of the neuron differs. It is common practice in the machine learning community to normalize the data, before passing them through the neural network. That way one can avoid unit dependencies and mistakenly weigh features with higher values as more important[50]. To normalize the data, the minimum and maximum values of the training dataset of each feature are used. Then, the test dataset is normalized based on the values of the training dataset.
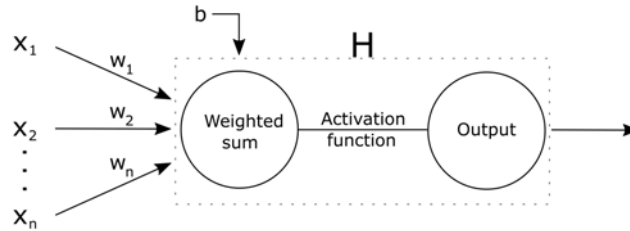

Figure 2.2: Illustration of a single artificial neuron, where X_n are the input data, w_n are the weights of each connection, b is the bias and H is the neuron (*i.e.*, perceptron).

In this work, two activation functions were utilized in the neural network, *softplus* (Equation (2.29)) and *swish* (Equation (2.30)):

$$f_{\text{softplus}}(x) = \frac{1}{\beta}ln(1 + e^{\beta x}) \tag{2.29}$$

and,

$$f_{\text{swish}}(x) = x\frac{1}{1 + e^{-\beta x}} \tag{2.30}$$

where, β is a scalable, trainable parameter.

In Figure 2.3, the activation functions are plotted, for $\beta = 1$. It is observed that the neuron will return a zero value if the input is smaller than approximately -3 and -5 for *softplus* and *swish*, respectively. Although the data are normalized from 0 to 1, the probability of the neuron being activated depends on the values after the weight and bias are accounted for.
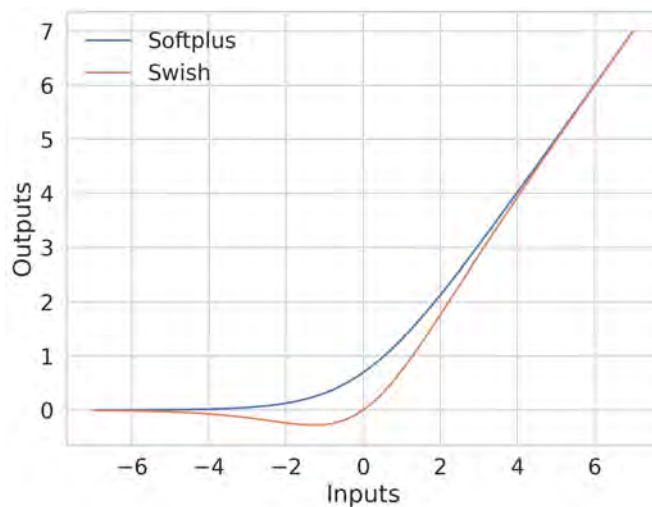

Figure 2.3: Activation functions that were used in the deep neural network in this work. Blue, upper line: *softplus* function, orange, lower line: *swish* function. In both cases β was set equal to 1.

A neural network is considered shallow if it consists of 5 or fewer layers. Otherwise, it is referred to as a deep neural network. Depending on the application different neural network architectures are required. In Figure 2.4, the schematic form of a neural network is illustrated. The input parameters, X_n pass through the layers, H_n, and the final output, O is calculated. This output is called the *target feature* and refers to the predicted value of the neural network for a certain case.
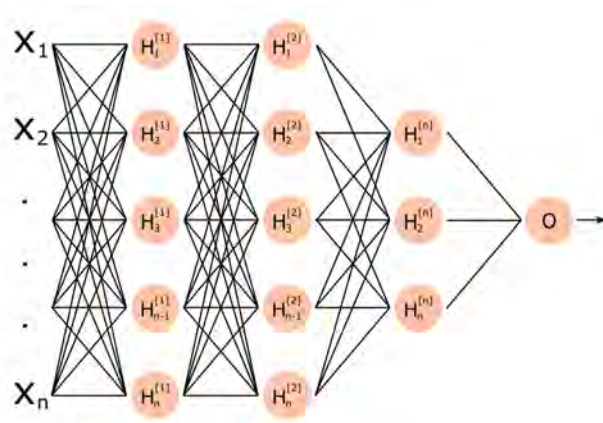
Figure 2.4: Schematic illustration of a neural network. The input data of a certain case, the neuron, and the predicted output (*i.e.*, target feature) are noted as X_n, H_n and O, respectively.

The evaluation of the training and the predictions can be performed by following the evolution of the mean squared error (MSE) and mean absolute error (MAE) with respect to the number of iterations (*i.e.*, epochs). That way, one can examine whether the learning and validation are performed equally well, or if there are inconsistencies. If the learning and validation curves do not overlap, it means that the model may have either overtrained (*i.e.*, performs better on the learning dataset, in comparison to the validation one) or undertrained (*i.e.*, performs better on the validation dataset, in comparison to the training one), and means to avoid that should be considered.

2.5 Vibrational spectroscopy

Atoms that are chemically bonded, forming a molecule, can move relative to each other in different motions, called molecular vibrations, or vibrational modes. These motions include stretching (changes in bond lengths), bending (changes in bond angles), and torsional (twisting around a bond) motions. Each motion has energy associated with it, which is determined by the masses of the atoms and the strength of the chemical bonds[51].

Raman spectroscopy is used for the study of molecular vibrations, rotations, and other low-frequency modes in a system. It is based on the Raman effect, which in the result of inelastic scattering of monochromatic light, typically from a laser source. When light interacts with a molecule, most photons are scattered elastically (*i.e.*, Rayleigh scattering), meaning that there may be a change in direction, but not in energy. However, a small fraction of the light undergoes inelastic scattering, resulting in photons that are either shifted to higher or lower energies of those corresponding to the vibrational energy levels of the molecule (*i.e.*, Raman effect)[52].

The resulting Raman spectrum displays these energy shifts as peaks at specific wavenumbers, each representing a specific vibrational mode of the molecule. The intensity and position of these peaks provide a molecular fingerprint that can be used for the identification and characterization of molecules and structures. Raman spectroscopy is particularly useful for studying non-polar bonds and aqueous solutions. This is because non-polar bonds exhibit strong Raman signals, while water molecules do not, allowing molecules present in an aqueous solution to be investigated[53].

2.6 Nuclear magnetic resonance techniques

Nuclei with an odd number of protons or neutrons have an intrinsic property called spin, which gives them a magnetic moment, m. The most common example is the ^{1}H, for which, as the mass number denotes, the nucleus has one proton. When a sample containing these nuclei is placed in a strong external magnetic field (B_0), the nuclear spins align with or against the direction of the field, creating distinct energy states. Furthermore, these nuclei resonate at a characteristic frequency, called the Larmor frequency, ω_0, which is defined as:

$$\omega_0 = \gamma B_0 \tag{2.31}$$

where γ is the gyromagnetic ratio of the nucleus.

Applying radiofrequency (RF) pulses at the Larmor frequency, causes transitions between these energy states. The nuclei absorb and subsequently relax back to their

initial state, leading to the re-emission of energy in the form of an electromagnetic wave (RF energy), which is detected and produces a nuclear magnetic resonance (NMR) signal. Depending on the neighboring atoms of the formally excited protons, the electronic environment close to the nucleus will differ, resulting in a slight change in the magnetic field experienced by the nucleus. This difference gives rise to a shift in the resonance frequency, called a chemical shift, and provides information about the chemical environment and the molecular structure[54].

Magnetic resonance imaging (MRI), commonly associated with the medical procedure, presents the same working principle as NMR spectroscopy while allowing the spatial encoding of molecular information. This is achieved by applying magnetic fields along the x, y, and z axes (gradient magnetic fields), which allow the encoding of positional information into the NMR signal. Moreover, by systematically varying the gradients, the location of the emitted signals can be precisely mapped, enabling the reconstruction of an image[55].

2.7 X-ray scattering

In X-ray scattering photons with wavelengths, λ, below 10 nm are used as a radiation source, allowing the characterization of structures at the nanoscale[56]. Electrons scatter X-rays, consequently, an incident X-ray wavevector k_i, will be scattered as a scattering wavevector k_f, depending on the electron density of the material[57]. The magnitude of the wavevector, $|k|$ is expressed as:

$$|k| = 2\pi/\lambda \tag{2.32}$$

The intensity of the scattered radiation, also known as the scattering vector q, is expressed as:

$$q = k_f - k_i \tag{2.33}$$

During an elastic scattering the magnitude of the incident wavevector $|k_i|$, is equal to the magnitude of the scattered wavevector $|k_f|$. In that case, the magnitude of the scattering vector is:

$$q = \frac{4\pi}{\lambda} \sin \theta \qquad (2.34)$$

By applying the Bragg's law the above equation becomes:

$$d = \frac{2\pi}{q} \qquad (2.35)$$

This equation allows the determination of distances, d, between for example lamellar layers in a sample from the scattering vector, q, at the first order Bragg's peak.

Depending on the distance of the detector from the sample, different length scales can be investigated. These are typically called small-angle X-ray scattering (SAXS) and wide-angle X-ray scattering (WAXS), for long and short distances, respectively.

3

Methods

3.1 Construction of the acoustic levitators

The scaffolds of the customized acoustic levitators were designed in the open-source software OpenScad and were 3D printed (Ultimaker S3, Netherlands) using polylactic acid (PLA). A multiple-transducers acoustic levitator consists of two opposing halves (Figure 1.1b). The transducers that are present on the same half need to have the same polarity. For that reason, an oscilloscope was used to determine the polarity before wiring them together through soldering, as described in Reference[25]. Through an Arduino Uno board, the operating frequency of transducers was set at 40 kHz, and the driving signal was amplified with an L298 N H-bridge.

The phase of the driving signal, of the two opposing halves, can be controlled. In this thesis two cases were examined: i) phase difference of $\Delta\phi = 0$ rad (*i.e.*, in phase), and ii) phase difference of $\Delta\phi = \pi$ rad (*i.e.*, phase opposition). This phase difference was applied by simply switching the polarity of the two channels on the L298 N board.

3.2 Simulations of acoustic levitators

The simulations of the customized acoustic levitators were performed through the Python library *Levitate*[37], developed by Carl Andersson, at Chalmers[58]. Initially, the positions of the transducers in space were defined in Cartesian coordinates. Following, the directivity pattern of the transducers (*i.e.*, pattern of acoustic wave propagation from a sound source) was described as a circular ring, and the parameter p_0, which defines the acoustic pressure an ultrasonic transducer induces at 1 m, was arbitrarily set to 1 Pa.

3.2.1 Acoustic pressure field

The acoustic pressure field was calculated as the summation of the individual acoustic pressures each transducer generates, as expressed in Equation (2.1). The cases of the opposing halves operating in phase and phase opposition were simulated.

3.2.2 Acoustic radiation force

The acoustic radiation force was simulated for the case of a spherical polystyrene particle with a diameter of 1 mm from the class *levitate.fields.RadiationForce*[37], in accordance with Sapozhnikov and Bailey[59], as formulated in Reference[58].

The spatial gradient of the Gor'kov potential[42], which is a simpler expression of the acoustic radiation force, was simulated for the case of a levitating polystyrene particle with a diameter of 1 mm, based on the Equation (2.7).

3.2.3 Axial trap stiffness

The axial trap stiffness was calculated along the horizontal and vertical directions at the anti-node through the class *levitate.fields.RadiationForceGradient*[37].

3.3 Evaluation of experimental performance

3.3.1 Operating frequency

The operating frequency of the ultrasonic transducers was adjusted using a Si5351A (Adafruit) module as a clock generator, which was controlled by an Arduino board. The signal was then amplified through an L298 N H-bridge. The voltage was kept constant and the operating frequency of the transducers was varied from 36 kHz to 41 kHz. Then, the current consumption was measured on the main line of the circuit using a magnetoresistive current sensor module based on an ACS70331 chip, connected to the Arduino board. The Arduino and the power supply were controlled by a computer, through a serial port[24].

Two different array configurations were investigated; single-side independent arrays (Figure 3.1a) and coupled arrays forming a cavity (Figure 3.1b). The frequency sweeps were performed at three voltages (7 V, 10 V, and 12 V), when the opposing halves were operating either in phase ($\phi = 0$ rad), or in phase opposition ($\phi = \pi$ rad). Each measurement was repeated three times.

Figure 3.1: Array configurations of an acoustic levitator of a) single-side independent arrays, and b) coupled arrays forming a cavity.

3.3.2 Levitation stability

The spatial stability of a levitating object was examined at three different voltages (7 or 7.5 V, 10 V, and 12 V) by capturing photographs of Milli-Q (resistivity of 18.2 MΩ·cm, at 25 °C, Merck Group, Sweden) water droplets through a digital camera (acA1440-220um, Basler, Germany) that was operating at 1 frame per second (fps), over a period of 10 min. From the photographs, the volume, and the coordinates of the center (x_c, z_c) of the droplets were extracted. The volume of the droplets was in the range of 0.5 to 5 μL. The measurements were repeated three times and the moving standard deviation, over a sliding window of length equal to 10 frames was calculated. This allowed observing potential dependencies between the volume and the spatial stability of the levitating droplet. The average standard deviation of the three sets of measurements was plotted with respect to the applied voltage.

3.3.3 Levitation capacity

The minimum strength generated by the acoustic field of each levitator was experimentally evaluated in the normal (*i.e.*, vertical) and perpendicular (*i.e.*, horizontal) orientation by determining the minimum voltage, V_{min} required to levitate a solid, spherical silica bead with mass, $m = 7$ mg and diameter, $d = 2.07$ mm. For the normal orientation (Figure 3.2a), the silica bead was levitated at 8 V and then the voltage was gradually decreased until the silica bead was no longer able to be suspended. Regarding the perpendicular orientation (Figure 3.2b), the starting voltage was set at 25 V and was gradually reduced. The measurements were repeated three times and the standard deviation was calculated.

The levitation force per voltage was calculated based on the weight of the silica bead over the applied voltage as:

$$C_{lev} = \frac{m \cdot g}{V_{min}}, \qquad \text{with} \quad V \geq 5 \text{ V} \tag{3.1}$$

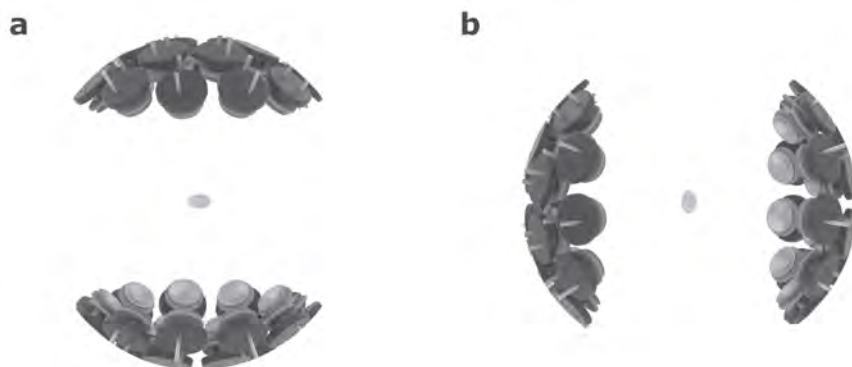where, m is the mass of the silica bead, g is the acceleration constant (9.81 m/s^2).

Figure 3.2: (a) Normal (*i.e.*, vertical) operating orientation of an acoustic levitator, and (b) perpendicular operating orientation to the normal one (*i.e.*, horizontal) of an acoustic levitator.

3.4 Surface and interfacial tension measurements

The surface tension of the surfactant solutions was measured through the pendant drop method, using the Attension Theta optical tensiometer (Biolin Scientific, Finland). The measurements were conducted at room temperature. For the case of surfactant solutions, the measurements were performed on a minimum of 10 droplets, formed using a 0.718 mm (22 gauge) stainless steel needle. The droplets were left to equilibrate for about one minute before starting the measurements that would last for 2 min, following the practice described in Reference[60]. A monochromatic digital camera was used to record images of droplets and the surface tension was determined by fitting the Young-Laplace equation on the contour of the droplet. The surface tension of a solution was determined by averaging the surface tension values of the 10 droplets.

For the interfacial tension measurements, a 1x1 cm quartz cuvette was used. The cuvette was filled halfway with either water or hexadecane (with 0, or 5 cycles of purification). The measurements were performed on a minimum of 10 droplets of the opposite phase with a 0.718 mm needle, thus acquiring the oil in water and water in oil interfacial tension measurements. An average equilibration time of 2 min was used. For the case of water in oil measurements, a hooked needle with a 0.718 mm diameter was used. In that case, the calibration was repeated while the needle was

immersed in the liquid. In all cases, the Young-Laplace equation was fitted on the contour of the droplets to acquire the values.

3.5 Machine learning

3.5.1 Acquisition of experimental data

Series of aqueous solutions of sodium dodecylsulfate (SDS), cetyltrimethylammonium bromide (CTAB), and TritonX-100 (10^{-7} - 10^{-1} M) were prepared in Milli-Q water, at 23 °C. The aqueous surfactant solutions were stored at room temperature, and the acoustic levitation measurements were acquired within a maximum of three days after the solution was prepared. A disposable steel needle (Sterican, Braun, Fisher Scientific, USA) attached to a disposable plastic syringe (Injekt, Braun, Fisher Scientific, USA) were utilized to introduce a droplet into the central acoustic node. Photographs of the levitating droplet were captured through a digital camera (acA1440-220um, Basler, Germany) with a frame rate of 1 fps, while the voltage varied with a rate of approximately 0.05 V/sec, over a period of 30 min. A Python code was developed to detect the contour of the droplet, determine the coordinates, and calculate various droplet characteristics, such as radius, volume, aspect ratio, position, *etc.*. Furthermore, the voltage, current, and time at which each image was taken were recorded. The measurements were repeated 3 times for each surfactant solution.

3.5.2 Preparation of experimental data

The extracted contours were corrected for tilting and relative position. The tilting was determined from the OpenCV Python library, and the related position of a droplet was determined by setting the center of each droplet at the (0,0) coordinate.

The chosen input features were: 175 polar radii, r, for constant polar angle, ϕ, the voltage, the current, and the relative position of the center of the contour along the z-axis, while the surface tension was set as the target feature.

A total of more than 50,000 contours of levitating aqueous surfactant droplets were used for the training and evaluation of the DNN. These contours belonged to a series of surfactant solutions that covered well the adsorption isotherm of each surfactant (SDS, CTAB, and TritonX-100). Eighty percent (80%) of the contours were used as the training dataset, with 20% of the training data set aside as the validation dataset. The remaining 20% of the contours were used as the test dataset.

The input features of the training dataset were normalized column-wise from 0 to 1. Then, the test subset was normalized based on the range of the training features. The polar radius, r, was normalized with respect to the minimum and maximum values among all the droplets in the training subset so that the size ratios could be retained.

3.5.3 Architecture of deep neural network

The architecture of the DNN that was developed for the determination of surface tension of levitating droplets is reported in Table 3.1. The DNN consisted of 8 layers, with 50, 40, 30, 20, 15, 10, 5, and 1 neuron(s). In the layers with an odd number (1, 3, 5, and 7) the activation function swish was used, while the activation function softplus was applied in the layers with an even number (2, 4, 6, and 8). The loss function was monitored through the MSE, and the optimization function Adam was used.

Table 3.1: Architecture of the developed neural network for the prediction of surface tension of self-standing droplets. The output shape defines the number of neurons present in each layer and the number of parameters are shown in the last column. The total number of trainable parameters was 13,376.

Layer (type)	Output Shape	No. Parameters
Layer 1 (Dense)	(None, 50)	8,950
Layer 2 (Dense)	(None, 40)	2,040
Layer 3 (Dense)	(None, 30)	1,230
Layer 4 (Dense)	(None, 20)	620
Layer 5 (Dense)	(None, 15)	315
Layer 6 (Dense)	(None, 10)	160
Layer 7 (Dense)	(None, 5)	55
Layer 8 (Dense)	(None, 1)	6

3.5.4 Evaluation of neural network

The MSE and MAE of the training and validation subsets were plotted with respect to the number of iterations (epochs) performed during the training. The surface tension predictions that the model generated were compared to the surface tension values determined through the pendant drop method (*i.e., True values*, in machine learning terminology). Additionally, the error distribution was plotted to better evaluate the error range of the model.

3.5.5 Feature importance

A permutation feature importance algorithm, introduced by Fisher, Rudin, and Dominici[61] was applied to investigate the influence of each feature on the predictions. Initially, the MAE of the neural network without permuting the features was determined by predicting on the test dataset, after training. Following, the first feature was permuted by shuffling the specific column of the test dataset. The prediction was repeated and the resulting MAE was recorded. The same procedure was repeated for all features. The procedure was repeated three times. The feature importance was calculated by subtracting the MAE of the original test dataset from the MAE of each permuted feature. If the error increased significantly after a feature was permuted, it indicated that the feature had a high influence on the predictions of the neural network. It should be noted that this analysis is used as a tool to examine the choice of features that the DNN makes, and whether this choice has a physical meaning. It is not used as a means to add interpretability to the neural network.

3.6 Optical microscopy

An Axio Imager Z2m, optical microscope (Zeiss Group, Germany) was used for the acquisition of images through the 10-, 40-, and 50-times magnification lens. A microscope glass slide (Avantor 631-1551, VWR International, USA), and a borosilicate cover glass (631-0124, 22x22 mm2, VWR International, USA) were used for the examination of the samples.

3.7 Contact-free vibrational spectroscopy

An InVia Reflex Raman spectrometer from Renishaw (Wotton-under-Edge-Gloucestershire, UK) with a 785 nm diode laser as the excitation source was used for the acquisition of Raman spectra. The spectrometer was calibrated using a Si wafer by setting its first-order vibrational mode at 520.6 cm^{-1}. The acoustic levitator Mk3 was used in this study. Initially, the levitator was operating along the vertical configuration (Figure 3.2a), and a droplet of water was deposited within the central acoustic node through a disposable plastic syringe attached to a disposable metallic needle. Then, a droplet of hexadecane was added onto the levitating droplet of water through 1 mm in diameter capillary attached to a Hamilton glass syringe (Fisher Scientific, Sweden). Following, the levitator with the 2 droplets being simultaneously levitating were manually transported and titled horizontally (Figure 3.2b) to fit under the Raman microscope. The droplet was detected under the microscope through a 5x magnification Leica objective with a numerical aperture (NA) of 0.12. A series of 10 spectra with a 5 sec spectral acquisition time was recorded by applying a 15 W power (5% static), in the spectral band region 100 cm^{-1} to 3400 cm^{-1}. The average intensity was calculated from those 10 spectra.

3.8 Contact-free magnetic resonance and imaging

A super wide bore (89 mm) Bruker Avance III 300 MHz ^1H (7.05 T) equipped with a 66 mm probe, set in a static gradient system for imaging was used. The shimming was performed on a 5 mm diameter glass tube containing the sample of interest. A mechanical lift was built to transport the acoustic levitator with the levitating sample at the detection zone of the MRI probe. Manual tuning and matching were performed while the acoustic levitator was operating, with and without a levitated droplet. The experimental details of the recorded magnetic resonance images and spectra can be found in the Methods section of Paper IV.

3.9 Contact-free X-ray scattering

SAXS (Small Angle X-Ray Scattering) and WAXS (Wide Angle X-Ray Scattering) analyses were conducted using a Xeuss 2.0 instrument (Xenocs, France) equipped with a Cu Kα radiation source (wavelength of 1.54 Å) and a PILATUS3 detector (Dectris, Switzerland). The detector was positioned at distances of 975 mm or 1000 mm for the SAXS measurements on levitating droplets and capillaries, respectively. For the WAXS measurements, the detector was positioned at distances 326 mm, or 340 mm for the levitating droplets and capillaries, respectively. A collimated beam size of 800 μm was employed, resulting in q-ranges of 0.011 Å^{-1} to 0.62 Å^{-1} for capillary measurements and 0.015 Å^{-1} to 0.63 Å^{-1} for levitation measurements in SAXS. In WAXS, the q-range was 0.043 Å^{-1} to 1.65 Å^{-1} for capillaries and 0.039 Å^{-1} to 1.65 Å^{-1} for levitation. Glass capillaries of 1.5 mm diameter were used and placed on a sample holder for capillary measurements, each lasting an hour. Scattering from the empty beam, empty capillary, and dark field was measured and subtracted from sample scattering, considering their relative transmissions. The scattering vector, q, was normalized with respect to the incident beam intensity to obtain absolute units (cm^{-1}). Levitation measurements with a duration of 15 min were carried out with and without CO_2 exposure. Additionally, kinetic measurements were conducted at 5, 15, and 25 min post-droplet deposition in the central acoustic node during CO_2 exposure. The scattering originating from the empty beam and dark field was subtracted while considering their relative transmissions.

4

Results and discussion

4.1 Customized acoustic levitators (Paper I)

Acoustic levitators that utilize multiple transducers offer great design flexibility as parameters such as the number, arrangement, and phase of the transducers, *etc.*, can be adjusted to customize them for different applications. In Paper I[24], three acoustic levitators, namely Mk1, Mk2, and Mk3, which satisfied the demands of practical applications in terms of size, stability, and levitation strength, were developed and evaluated through simulations and experiments.

In the case of acoustic levitator Mk1 (Figure 4.1a and Figure 4.2a), 17x2 ultrasonic transducers were placed in a concentric arrangement. The distance between the opposing array, L, was 52.1 mm, and the opening angle, θ, was 43°. The design was more compact in comparison to TinyLev[25], aiming to create a stronger acoustic field by concentrating the acoustic radiation forces in a more confined space. The size of the second design, Mk2 (Figure 4.1b and Figure 4.2b) was further decreased in comparison to Mk1. Levitator Mk2 consisted of 12x2 transducers; the plastic casing of the transducers was removed, to increase the density of the transducers in plane. The distance between opposing arrays, L, was 38.1 mm, and the opening angle, θ, was 47°. As shown in Figure 4.2a-b, the arrangement of the transducers in the cases of Mk1 and Mk2 was concentric, while for levitator Mk3 (Figure 4.1c) the transducers were placed in a hexagonal arrangement. This led to maximum packing of the transducers,

which aimed at increasing further the performance by increasing locally the acoustic pressure around the node. Levitator Mk3 consisted of 18x2 transducers. The distance of opposing arrays, *L*, was 43 mm, and the opening angle, θ, was 50°. The opposing planes were rotated by 60° with respect to each other so that the transducers were positioned symmetrically around the central node. In all cases, the transducers were placed on a concave plane, with the aim to increase the acoustic forces locally as shown by Adamowski *et al.*[32]. A more detailed description of the design parameters can be found in Table 1, Paper I[24].

4.1.1 Simulation of acoustic pressure field

The Python library *Levitate*[37] was used for simulating the acoustic pressure fields of the customized acoustic levitators. In Figure 4.1d-i, and Figure 4.2d-f, the simulations of the acoustic pressure fields, along the *xz*, *yz*, and *xy* planes are shown. It is observed that acoustic levitators Mk1 and Mk2 present equally high acoustic pressure along the *xz* and *yz* planes (∼1200 Pa). This shows that by adjusting the cavity length, it is possible to achieve the same acoustic pressure level with fewer ultrasonic transducers. Additionally, it is evident that the acoustic pressure fields of Mk1 and Mk2 in the *xz* and *yz* planes are identical due to the symmetrical, concentric arrangement of the transducers along the opposing planes. In comparison, the acoustic pressure field of acoustic levitator Mk3 along the *xz* and *yz* planes (Figure 4.1d-i) exhibited different patterns, due to the hexagonal arrangement of transducers and the 60° shift between the transducer planes. More importantly, Mk3 presented the highest acoustic pressure compared to the previous designs. This is attributed to the higher packing density of the transducers resulting from the hexagonal arrangement.
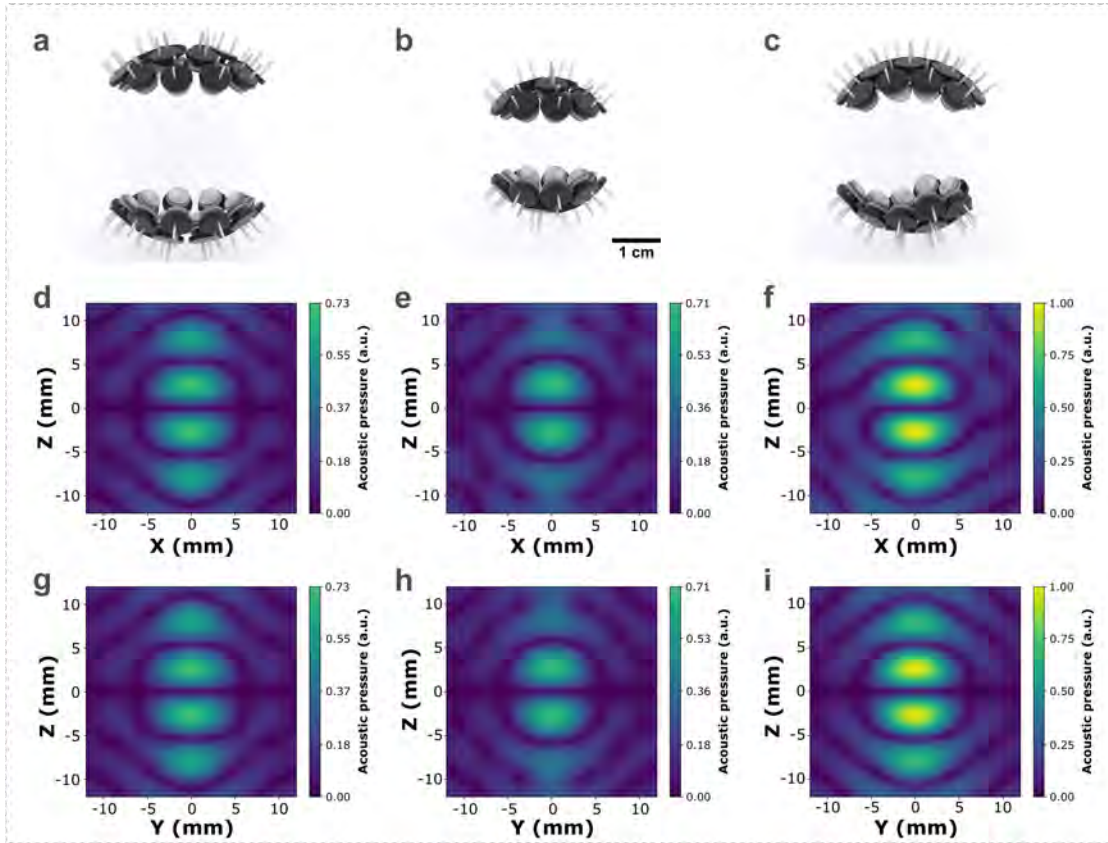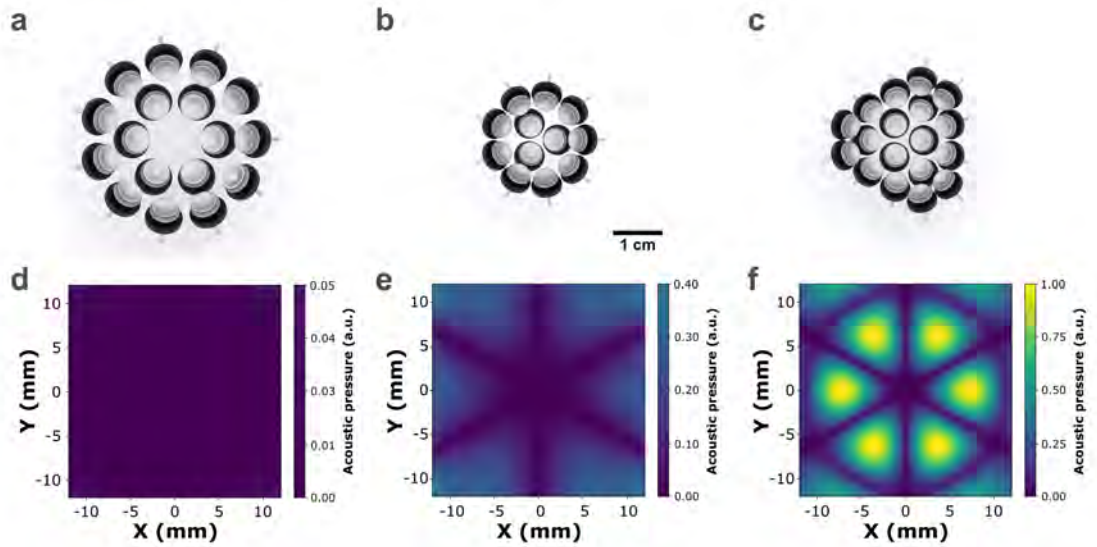
Figure 4.1: (a-c), Photorealistic rendering of acoustic levitators Mk1, Mk2, and Mk3, respectively, as viewed from the front (d-f) 2D simulations of acoustic pressure fields along the *xz* plane, and (g-i) *yz* plane. The acoustic pressure is normalized with respect to the maximum acoustic pressure of the acoustic levitator Mk3. Reproduced with permission from Reference [24].

Levitator Mk3 presented the highest acoustic pressure along the *xy* plane, followed by Mk2, while Mk1 exhibited the lowest acoustic pressure (Figure 4.2d-f). Furthermore, it is observed that the central area where the acoustic pressure is close to zero can be approximated by a circle with a radius of approximately 2.5 mm for Mk3 and approximately 8.0 mm for Mk2. Hence, the Mk3 design generated stronger lateral forces closer to the acoustic node, owning to the higher opening angle, θ [24].

Figure 4.2: (a-c), Photorealistic rendering of acoustic levitators Mk1, Mk2, and Mk3, respectively, as viewed from the top, (d-f) 2D simulations of acoustic pressure fields along the *xy* plane. The acoustic pressure is normalized with respect to the maximum acoustic pressure of the acoustic levitator Mk3. Reproduced with permission from Reference [24].

4.1.2 Distance of opposing arrays and operating frequency

As mentioned in Chapter 2, the optimum operating frequency of ultrasonic transducers may shift depending on the driving voltage. The performance of an acoustic levitator worsens the farther away from the resonant frequency it operates, simply because the transducers are not operated properly. Consequently, it is important to evaluate to what degree the optimum operating frequency is affected by the voltage applied. Furthermore, since ultrasonic transducers act both as emitters and receivers of acoustic waves, two configurations were defined where the two transducer planes were either opposing or not each other (Figure 3.1). Moreover, for each configuration, the measurements were repeated while the two halves were operating with a phase difference of either 0 rad or π rad.

In Figure 4.3a-b, the current consumption of levitator Mk1 with respect to the operating frequency of the transducers, for the case where the opposing transducer halves

were in phase difference of π rad, and 0 rad, respectively, is presented. Primarily, a different pattern is observed, depending on the phase difference, and secondly, a slight shift in the frequency where the current reaches a maximum is observed as the driving voltage increases. This shift is more prominent in the case where the phase difference is π rad. In order to examine whether the different pattern is attributed to the wave interactions between the opposing halves, the same measurements were repeated while the two halves were not facing each other. In Figure 4.3c, it is shown that regardless of the phase difference the current consumption pattern remained the same, confirming the influence of the wave interactions on the transducers. Similar patterns were observed for all tree acoustic levitators as shown in the Supporting Information of Paper I[24].
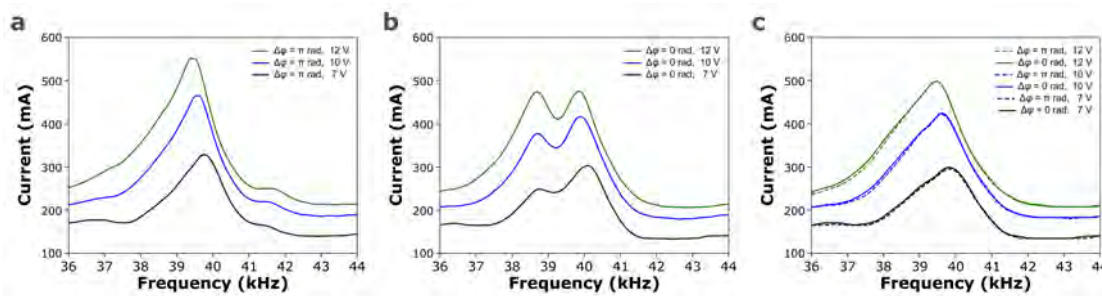
Figure 4.3: Current consumption of acoustic levitator Mk1 when a) the transducer halves are opposing each other with a phase difference of π rad, b) the transducer halves are opposing each other with a phase difference of 0 rad, c) the transducer halves are not interacting with each other and there is a phase difference of π rad (dashed line), and 0 rad (continuous line). Reproduced with permission from Reference [24].

In Figure 4.4a, the current consumption of acoustic levitator Mk3 at the resonant frequency of the transducers (40 kHz) with respect to the distance of opposing arrays, while the phase difference was either π rad or 0 rad is shown. In both cases of phase difference, the current consumption presented a damping oscillation pattern as the distance between the opposing arrays increased. Subsequently, a difference of half a wavelength, $\lambda/2$, was recorded between the two cases. To examine the effect of distance of opposing arrays, L to the acoustic pressure applied on a levitating object, a water droplet was levitated, and the aspect ratio was recorded, as the distance, L, increased. The aspect ratio of a levitating liquid droplet can be used as a direct means to the degree of acoustic force applied onto it. Aspect ratio of 1 corresponds to a

spherical droplet (*i.e.*, low acoustic pressure applied), and the lower the value becomes the more compressed the droplet is. In Figure 4.4, the lowest aspect ratio was found when the distance, *L*, was 43 mm, which also overlaped with the minimum current consumption of the levitator Mk3 when the operating frequency was 40 kHz. As the aspect ratio was the smallest, it indicated that the droplet was the most compressed at that distance, *L*, indicating maximum acoustic pressure for that configuration. Though counter-intuitive, in the study by Contreras and Marzo[33], it was also shown through a schlieren deflectometer that maximum acoustic pressure is found at minimum current consumption. As the distance of the opposing arrays increased, a mismatch between the pattern of the current consumption and the evolution of the aspect ratio was observed, due to the reduced influence of the acoustic pressure field on the droplet.
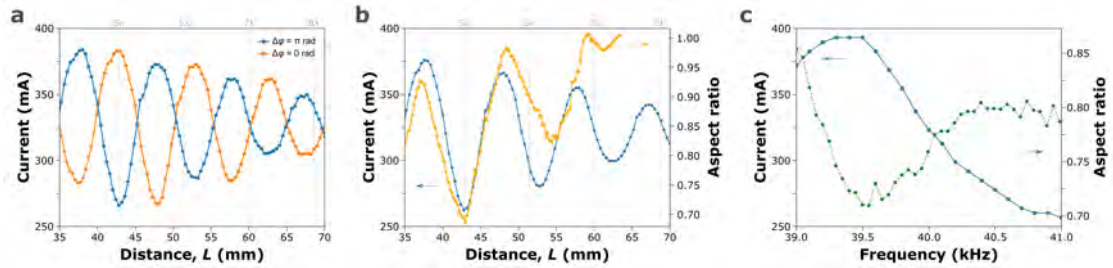
Figure 4.4: a) Current consumption of acoustic levitator Mk3, at 40 kHz, with respect to the distance of opposing arrays, *L*, while the opposing arrays were operating in phase difference of π rad (blue line) and 0 rad (orange line), b) comparison between current consumption of acoustic levitator Mk3, while the opposing arrays had a phase difference of π rad and aspect ratio of a water droplet with initial volume of 2 µL, with respect to the distance of opposing arrays, *L*, and c) Comparison between current consumption of acoustic levitator Mk3 (left *y*-axis; blue, continuous line) and aspect ratio of a water droplet with initial volume of 3.45 µL (right *y*-axis; green, dashed line), with respect to the operating frequency. In all cases, the driving voltage was set at 9.5 V. Reproduced with permission from Reference [24].

As shown in Figure 4.3a, by increasing the voltage, a shift in frequency at which the current reaches a maximum is observed. In Figure 4.4c, the operating frequency of the transducers was varied at a constant voltage. Moreover, a droplet of water was simultaneously levitating, to examine a potential change in the acoustic pressure applied onto the droplet. It was found that the current consumption reached a maximum when the operating frequency was approximately 39.5 kHz, which coincided with the minimum

aspect ratio (maximum applied acoustic pressure) of the droplet. Furthermore, an increase in aspect ratio was observed as the operating frequency deviated from the resonant frequency of the transducers at 40 kHz. These experiments indicated the influence of the distance L on the acoustic pressure applied onto a levitating object and the possibility of fine-tuning the applied acoustic pressure by adjusting the operating frequency.

4.1.3 Levitation capacity

The levitation capacity, C_{lev}, defined in Equation (3.1), is an empirical parameter, which allows the direct comparison of the levitation strength of the levitators. As mentioned in Chapter 2, the driving voltage is correlated to the applied acoustic pressure. Consequently, the lower the driving voltage that is required to keep an object with a certain weight aloft, the higher the overall generated acoustic pressure, thus the capacity to levitate.
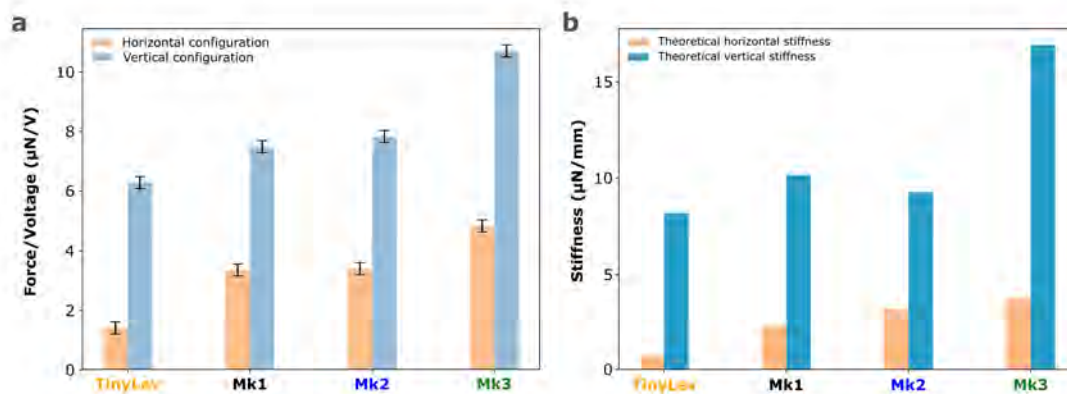
Figure 4.5: Comparison of the a) experimentally determined levitation capacity, and b) simulated axial trap stiffness, of acoustic levitators TinyLev, Mk1, Mk2, and Mk3 while operating along the vertical operating orientation (blue columns) and horizontal operating orientation (orange columns), and phase difference of opposing arrays of π rad. Reproduced with permission from Reference [24].

For this measurement, a silica bead with a mass of 7 mg was levitated at high voltage with TinyLev, and the 3 customized acoustic levitators, while operating in vertical

(Figure 3.2a), or horizontal configuration (Figure 3.2b). Then, the driving voltage was gradually decreased until the silica bead ceased to levitate. In Figure 4.5a, it is shown that TinyLev presented the overall lower levitation capacity, followed by Mk1 and Mk2 with similar levels, and Mk3 with the highest levitation capacity of all. In Figure 4.5b, the simulated axial trap stiffness of each levitator along the horizontal (x, y axes), and the vertical (z axis) are presented. This parameter expresses the force required to cause a 1 mm displacement, around the acoustic node, and is found to correlate well with the levitation capacity.

4.1.4 Spatial stability

The spatial displacement of the levitated object over time was evaluated on water droplets over a period of 10 min, at three different voltages (7 or 7.5, 10, and 12 V). Examining this parameter with a liquid droplet allows the evaluation of the levitator for the intended use for physicochemical studies of soft matter, while potential volume dependencies between the stability and the levitating sample can be unraveled. In Figure 4.6, the average standard deviation of the center (x_c, z_c) of the levitated water droplets is plotted with respect to the applied voltage along the horizontal, x-axis (upper plot) and vertical, z-axis (bottom plot) movement. The acoustic levitator, Mk3, presented the least droplet displacement (*i.e.*, stability) along both the horizontal, x- and vertical, z-axes, followed by Mk1, Mk2, and TinyLev. In the case of displacement along the z-axis, the latter three acoustic levitators presented similar levels of displacement, while Mk3 exhibited higher stability, within a ± 10 μm range.

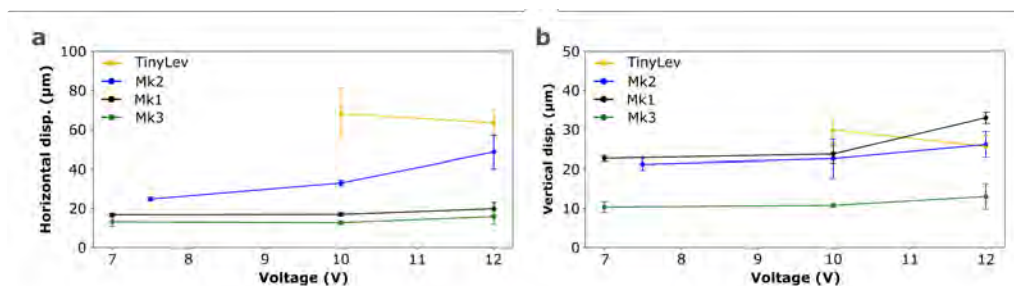**Figure 4.6:** The average standard deviation of the center (x_c, z_c) of levitated water droplets is plotted with respect to the applied voltage for acoustic levitators: TinyLev (orange), Mk1 (black), Mk2 (blue) and Mk3 (green), along a) the x-axis and b) the z-axis. Reproduced with permission from Reference [24].

Based on previous studies, the degree of spatial displacement of a levitating object depends on the axial trap stiffness and the curl forces within the trap[62]. Consequently, the level of acoustic forces around the acoustic trap and the pattern of the acoustic pressure field will have an influence. This may explain the lower stability of Mk2, in comparison to Mk1, along the *x*-axis, although higher lateral pressure was found based on the acoustic pressure field simulations in Figure 4.2e-f.

4.2 Contact-free determination of surface tension (Paper II)

As explained in Chapter 2, the acoustic pressure field influences the shape of a levitating liquid droplet. The degree of deviation from sphericity depends on the volume, acoustic pressure, and surface tension (Figure 2.1). The resulting droplet shape is the result of the balance of forces on the surface of the droplet. However, the main difficulty arises from determining accurately the applied acoustic pressure on the surface of the droplet. Moreover, theoretical models usually apply simplifications and conditions that may limit the accuracy and applicability of the model. On the other hand, machine learning can unravel patterns from data, without setting any preconditions.

In Paper II[63], the customized levitator Mk1 was used for the acquisition of a large experimental dataset, required for the training of a neural network. Initially, the data-driven approach was validated on *in-silico* data that were generated from Equations (2.25)-(2.26) with and without artificial noise. Then, the same neural network architecture was implemented on experimental data, which will be the focus of this section. The input features on which the neural network relied the most, and potential droplet size and deformation limitations on the prediction of surface tension were investigated.

4.2.1 Experimental data and machine learning predictions

In Figure 4.7a-c, the distributions of the surface tension, volume, and voltage of the chosen experimental data are shown. In Figure 4.7d, representative overlapping

contours of levitating droplets are presented. These contours are larger and deviate more from a circular shape, in comparison to the theoretical ones[63].

The accuracy of the ML predictions on the experimental data was evaluated in Figure 4.7e-f and Figure 4.8. In Figure 4.7e, the surface tension ML predictions were compared to the surface tension values measured through the pendant drop method. It was found that the majority of the predictions were in agreement with the pendant drop method. In Figure 4.7f, the error distribution of the ML predictions is shown, and the majority of the predictions were in the range of ± 2 mN/m, while the average MAE was 0.88 mN/m.
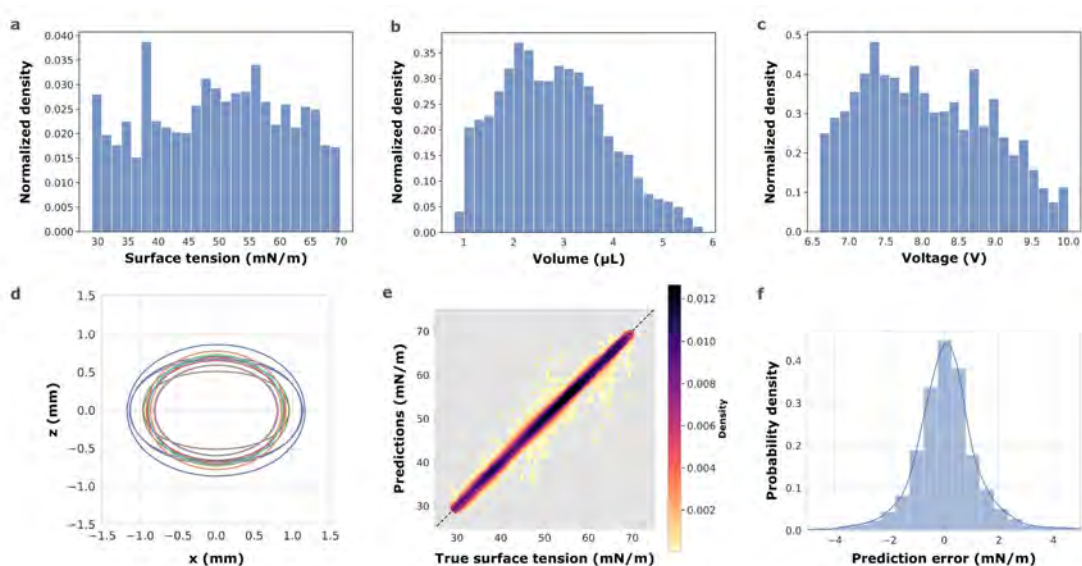
Figure 4.7: Data distributions of a) surface tension, b) volume, c) voltage of experimental data. d) Representative overlapping contours of experimental data. e) Comparison between the surface tension values measured through the pendant drop method (*x*-axis) and the surface tension values predicted through the ML algorithm (*y*-axis) on the test dataset (11,674 instances). f) Error distribution of the surface tension predictions the ML algorithm made on the test dataset (11,674 instances). Reproduced with permission from [63].

In Figure 4.8a-c, 100 randomly chosen ML predictions are plotted with respect to the adsorption isotherms of SDS, CTAB, and TritonX-100, respectively. Overall, the predictions cover the isotherm at a satisfactory level and the majority of the predictions

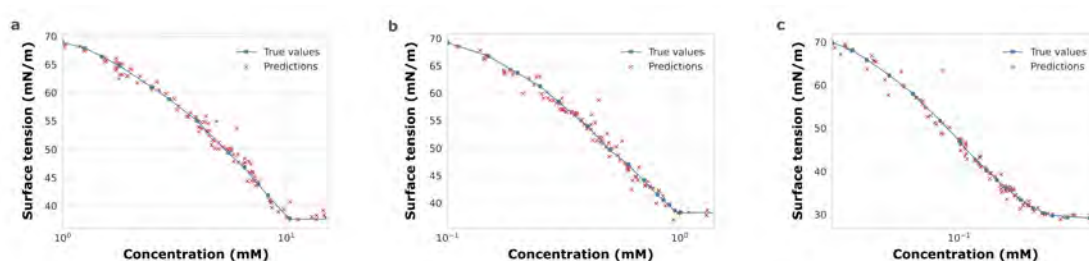appear to be in very good agreement with the measurements acquired with the pendant drop technique.

Figure 4.8: Comparison between the adsorption isotherm curves (*True values*) and 100 randomly distributed ML predictions of a) sodium dodecylsulfate (SDS), b) cetyltrimethylammonium bromide (CTAB), and c) octylphenol decaethylene glycol ether (TritonX-100). Reproduced with permission from [63].

4.2.2 Feature importance analysis

A permutation algorithm was applied to investigate the importance of the input data for the ML to reach the predictions. This algorithm mixed the order of one feature at a time and calculated the error of the predictions with the new order. The higher the acquired error after mixing the order of the feature, the more important the feature was considered, as it was an indication of the ML being dependent on that feature, to reach correct decisions. In Figure 4.9a, it is observed that the greatest influence originated cumulatively from the 175 radii describing the contour of the droplet, followed by the voltage, current, and vertical position in space. To investigate the influence of the exact coordinates on the predictions, the contour was color-coded based on the feature importance (Figure 4.9b). The contour points at the extremities (*i.e.*, top, bottom, right, left) of the droplet had the highest feature importance, which is expected since these points are affected the most as the volume, pressure, and surface tension vary. The other three input features are directly correlated to the value of acoustic pressure applied on the droplet, with the voltage being the most important.
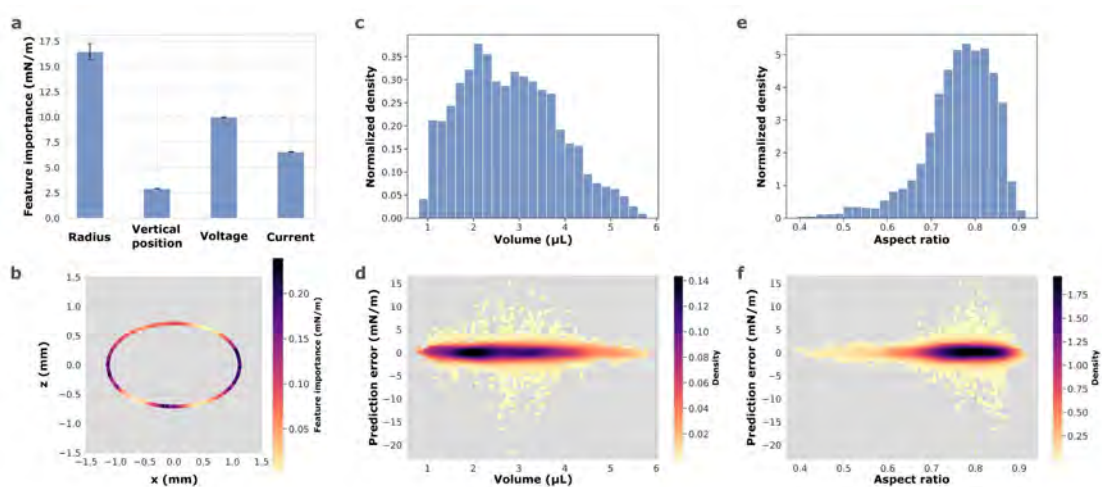
Figure 4.9: a)The influence of each feature that was input in the neural network is expressed as feature importance. b) The influence of each radius that defined the droplet contour on the machine learning predictions is color-coded. The darker the color of the point, the higher the influence on the prediction. c) Density distribution of volume in the test dataset. d) Prediction error with respect to the volume of the droplet. e) Density distribution of volume in the test dataset. f) Prediction error with respect to the aspect ratio of the droplet. Reproduced with permission from [63].

To identify potential error correlations between the predictions and the size or shape of the droplets, the data distributions of these parameters were compared to the MAE of the prediction with respect to the volume and aspect ratio (Figure 4.9c-f). The aspect ratio was used as a means to describe the deformation of the droplets, as the farther away it is from 1, the more oblate the shape of the droplet will be. In both cases, no clear correlation between the data distribution and the prediction error was drawn. The error was distributed in the same way as the data distribution, and a few outliers with high error were found in the regions with more data points. These errors may be attributed to droplet instabilities during the measurements. More importantly, the error when the volume was larger than 4 μL, and the aspect ratio was lower than 0.6, did not surpass 1 mN/m, which are cases where theoretical models could not be applied due to simplifications[41,46]. This indicates the applicability of this approach, and its potential to determine the CMC on a single droplet.

4.3 Contact-free macroscopic crystallization (Paper III)

In Paper III, a binary system of immiscible droplets was investigated through optical observations and Raman spectroscopy. Specifically, a droplet of water was levitated, and then a droplet of hexadecane was added onto it. The moment the two droplets came in contact, a macroscopic crystallization of the droplet of hexadecane was observed on the surface (Figure 4.10). Specifically, within the first 30 sec, approximately 20% of the surface became solid.
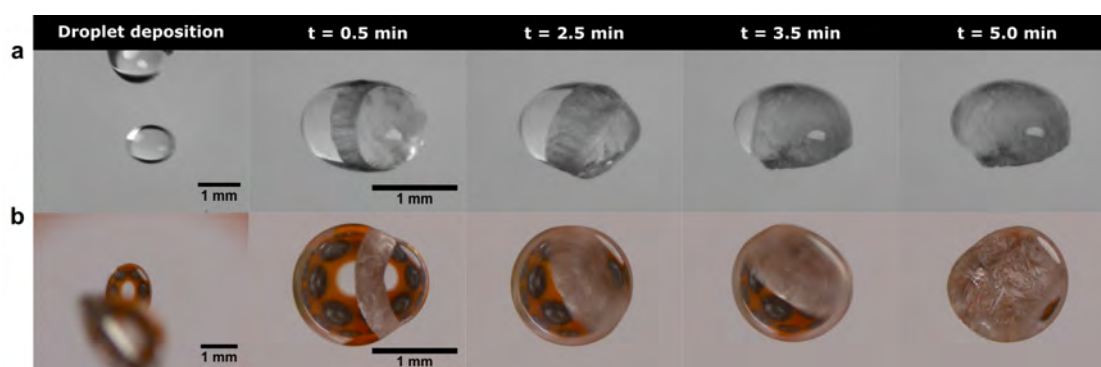
Figure 4.10: a) Side-camera view and b) top-camera view of the interfacial freezing of hexadecane under acoustic levitation, when the hexadecane droplet was in contact with the levitating droplet of water at different time periods, at 21 °C and 35% relative humidity. The orange color and the black circular parts in the photographs from the top camera are the color of the levitator and the ultrasonic transducers, respectively, that are present below the droplet. There is a hole at the centre of the levitator that is why the centre of the droplet has the same color as the background.

After approximately 5 min, the surface of hexadecane had fully solidified, while a couple of minutes later, the droplet began to melt back into a liquid (Figure 4.11). The melting process took place for approximately 3.5 min before the droplet of hexadecane was liquid again. Throughout this process, the droplet of water was evaporating, while after 8.5 min only a small volume was left.
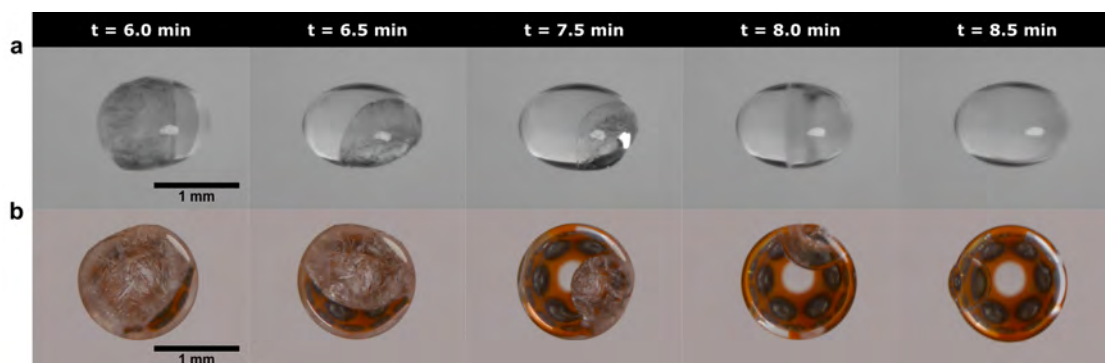
Figure 4.11: Continuation of side-camera view and b) top camera view of the acoustically levitated droplets of water and hexadecane, at 21 °C and 35% relative humidity. The droplet of hexadecane is melting back into a liquid.

An intriguing observation was that when a droplet of hexadecane was levitating and a droplet of water was added onto it, under the same experimental conditions (room temperature of 21 °C and relative humidity of 35%), no macroscopic surface crystallization took place (Figure 4.12). This was an unexpected result, that led to a surface and interfacial tension investigation.
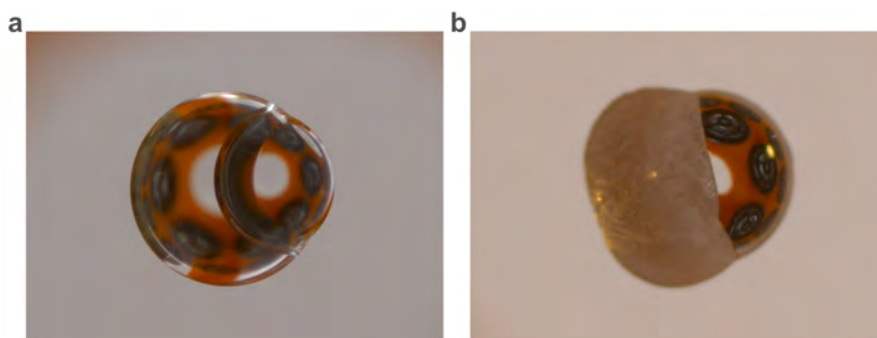
Figure 4.12: a) Top-camera view of liquid droplet of hexadecane (left) in contact with liquid droplet of water (right), after a droplet of water was added on a levitating droplet of hexadecane, and b) top-camera view of solid droplet of hexadecane (left) in contact with liquid droplet of water (right), after a droplet of hexadecane was added on a levitating droplet of water.

4.3.1 Effect of impurities in hexadecane

In the above observations, the hexadecane was used without further purification (99% pure hexadecane). Yet, previous publications have reported the presence of surface-active impurities in alkanes, leading to interfacial tension differences between the water in oil and oil in water measurements[64]. After performing the measurements, a 10 mN/m interfacial tension difference was indeed found, while a drift of approximately 3 mN/m was recorded, over a period of 2 min, indicating the presence of surface active impurities. The hexadecane in water interfacial tension values varied from 56.88 mN/m to 53.58 mN/m, and the water in hexadecane values varied from 48.19 mN/m to 45.07 mN/m; however, the surface tension values were steady for both liquids and equal to 27.23 $\pm$0.02 mN/m and 72.5 $\pm$ 0.08 mN/m for hexadecane and water, respectively.

Hexadecane was, therefore, passed through an aluminum oxide column, to remove the surface active impurities[64], and the interfacial tension measurements were repeated. After 5 purification cycles, the water in oil and oil in water interfacial tension measurements were constant and equal to 56.5 $\pm$ 0.1 mN/m, in both cases. The system was levitated at room temperature of 21 °C, and 32% relative humidity, and it was found that the macroscopic surface freezing took place regardless of the order of droplet deposition. This indicated that the interfacial tension difference may have had an influence on the macroscopic surface crystallization of hexadecane, due to surface energy and spreading differences.

4.3.2 Effect of humidity and temperature

Another important parameter is the humidity since it defines the rate of heat transfer from water to hexadecane during evaporation, leading to a cooling effect[65]. The cooling effect is more prominent in dry environments as the evaporation rate is higher. The relation between the humidity and the microscopic surface freezing of hexadecane was examined with the hexadecane that underwent 5 cycles of purification at 21 °C. It was found that the surface freezing of hexadecane occurred at relative humidity below 30%, regardless of the order of droplet deposition, indicating that the evaporation rate of water significantly impacted the formation of a solid phase.

Previous publications have claimed that the temperature of an acoustically levitated droplet of water was up to 11 K lower than the room temperature[66,67]. The temperature of a levitating water droplet and the two-droplets system was measured with an IR thermometer, with Mk1. It was found that the temperature was close to the room temperature that was measured with an electronic thermometer. Consequently, it was not purely the process of levitation, leading to water evaporation and therefore cooling, that led to the surface freezing of hexadecane.

Other publications have shown that alkanes form a hexagonally arranged monolayer at the air/alkane interface, 3 K above the melting point[47–49]. Through Differential Scanning Calorimetry (DSC) analysis the melting point of hexadecane was found to be at 18.5 ± 0.1 °C regardless of the number of purification-cycles, indicating that the surface active impurities did not have a significant influence on the bulk properties of the liquid. Following, the room temperature was increased from 21 °C to 25 °C and 30 °C, and in both cases, the freezing did not occur, indicating the critical role of the 3 K threshold.

4.3.3 Effect of the water to hexadecane volume ratio

As shown above, the evaporation rate of water significantly impacted the occurrence of the surface freezing of hexadecane. For that reason, the influence of the hexadecane-to-water volume ratio was examined as a contributing factor, when the room temperature was 21 °C and the relative humidity was 30%. In Figure 4.13, the volume of water appears to have a great influence on the maximum surface area of hexadecane being frozen, regardless of the order of droplet deposition. In the case where a droplet of hexadecane was deposited on a levitating droplet of water, the surface area of hexadecane was completely frozen when the volume of water was equal to the volume of hexadecane. Yet, a smaller fraction of surface area was frozen in the opposite order of droplet deposition overall. Moreover, the frozen part appeared to be less translucent, indicating either a thinner frozen layer or a different crystal phase.
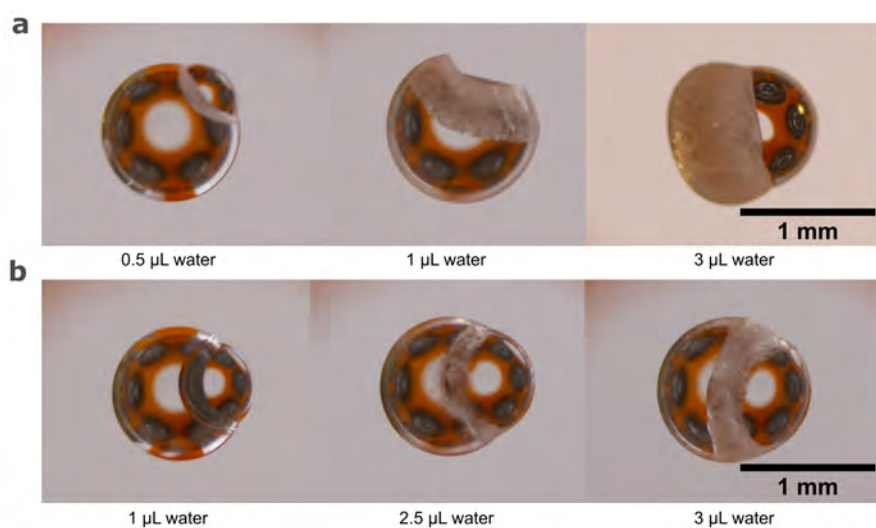
Figure 4.13: a) Maximum surface crystallization of a 3 µL droplet of hexadecane and various volumes of water when a) water was levitating first and hexadecane was added, and b) hexadecane was levitating first and water was added.

4.3.4 Contact-free vibrational spectroscopy

The phase transition was characterized in a contact-free manner by combining Raman spectroscopy and the acoustic levitator, Mk3. This levitator is stronger and more stable than Mk1[24], which allowed operating the device horizontally (Figure 3.2b) while both of the droplets were levitating. Two spectral band regions were examined: from 800 to 1600 cm^{-1}, and from 2600 to 3100 cm^{-1}, which can provide information about the crystal phase, and the physical state of hexadecane, respectively[68].

The Raman spectra shown in Figure 4.14a, vary in intensity, but appear to have the same pattern, regardless of the order of droplet deposition, which is characteristic for solid hexadecane[68]. This confirmed the presence of a solid phase in both cases. In Figure 4.14b, the Raman spectrum of the case where hexadecane was added on a levitating droplet of water (*i.e.*, water+hexadecane), is characteristic of a triclinic crystal state[68]. However, in the case where water was added on a levitating droplet of hexadecane, three peaks appeared in the spectral band region of $1367–1379$ cm^{-1}, and a difference in intensity ratio was recorded between the 1296 cm^{-1} and 1370 cm^{-1} peaks. This spectrum has not been reported before; yet, X-ray scattering studies and simulations support the presence of a transient rotator phase in hexadecane[48,69–71].
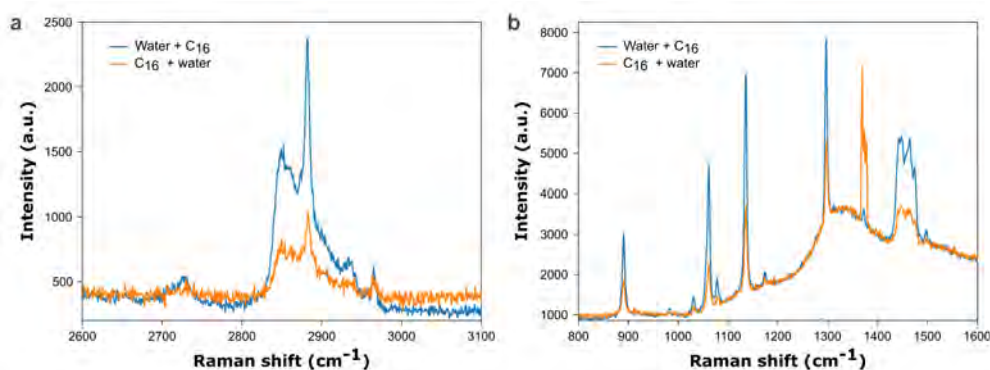
Figure 4.14: Raman spectra of the hexadecane/water system for the case when water was levitating first and hexadecane was added afterwards (blue) and in the opposite case (orange) showing the spectral range a) 2600 to 3100 cm⁻¹, and b) 800 to 1600 cm⁻¹.

Simulations have predicted that this rotator phase appears immediately upon freezing, and before transitioning into the more stable triclinic state[69]. In the Supporting Information of Paper III, it is shown that the peaks in the 1367–1379 cm^{-1} region disappeared upon melting of hexadecane and the triclinic phase appeared, indicating the transient nature and difficulty to capture this phase. It is probable that these peaks were visible here, due to a delayed freezing of hexadecane, owing to a relative humidity of 35%, which led to a slower heat transfer between the droplets.

The transition from a solid hexadecane to a liquid was also captured, by recording a series of Raman spectra (Figure 4.15a). During the melting process, the intensity and broadening of the peaks increased. The kinetics were quantified, by following the evolution of the 1296 cm^{-1} shift, which refers to the CH_2 twisting band. The width of the peak at t=0 min was set at 0% liquid, as the spectrum at the spectral band region of 2600 to 3100 cm⁻¹, after t=2 min, indicated the presence of a solid. In Figure 4.15b, it is shown that the melting process evolved at an exponential rate and the full transition occurred within approximately 3 min.
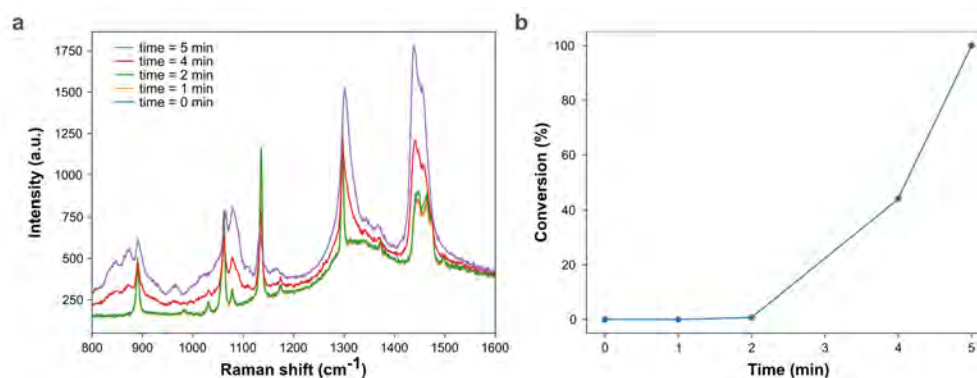
Figure 4.15: a) Raman spectra of the hexadecane/water system, while hexadecane was melting back into a liquid, and b) percent conversion of solid hexadecane (0%) into a liquid droplet (100%), calculated based on the width of the 1296 cm^{-1} shift, over time.

4.4 Contact-free magnetic resonance (Paper IV)

In Paper IV, a demagnetized version of the acoustic levitator Mk3 was developed and inserted into the 66 mm in diameter MRI bore of a 7.05 T magnet. A series of volatile and non-volatile solvents were studied, while the relation between the shape of the droplet and the chemical shift was established. It was also possible to follow molecular dynamics in real-time during evaporation.

4.4.1 Magnetic resonance imaging on self-standing droplets

In Figure 4.16a-c, MRI images of a levitating droplet of hexadecane are visualized by applying three different MRI pulse sequences, with an in-plane resolution of 312.5 μm/pixel, across the axial (*xy*), sagittal (*xz*), and coronal (*yz*) slices. In all cases, the droplet was well visible and no clear artifacts were present. However, in the case of RARE, the pulse input power was too high, which caused the droplet to burst, as shown in the Supporting Information of Paper IV.
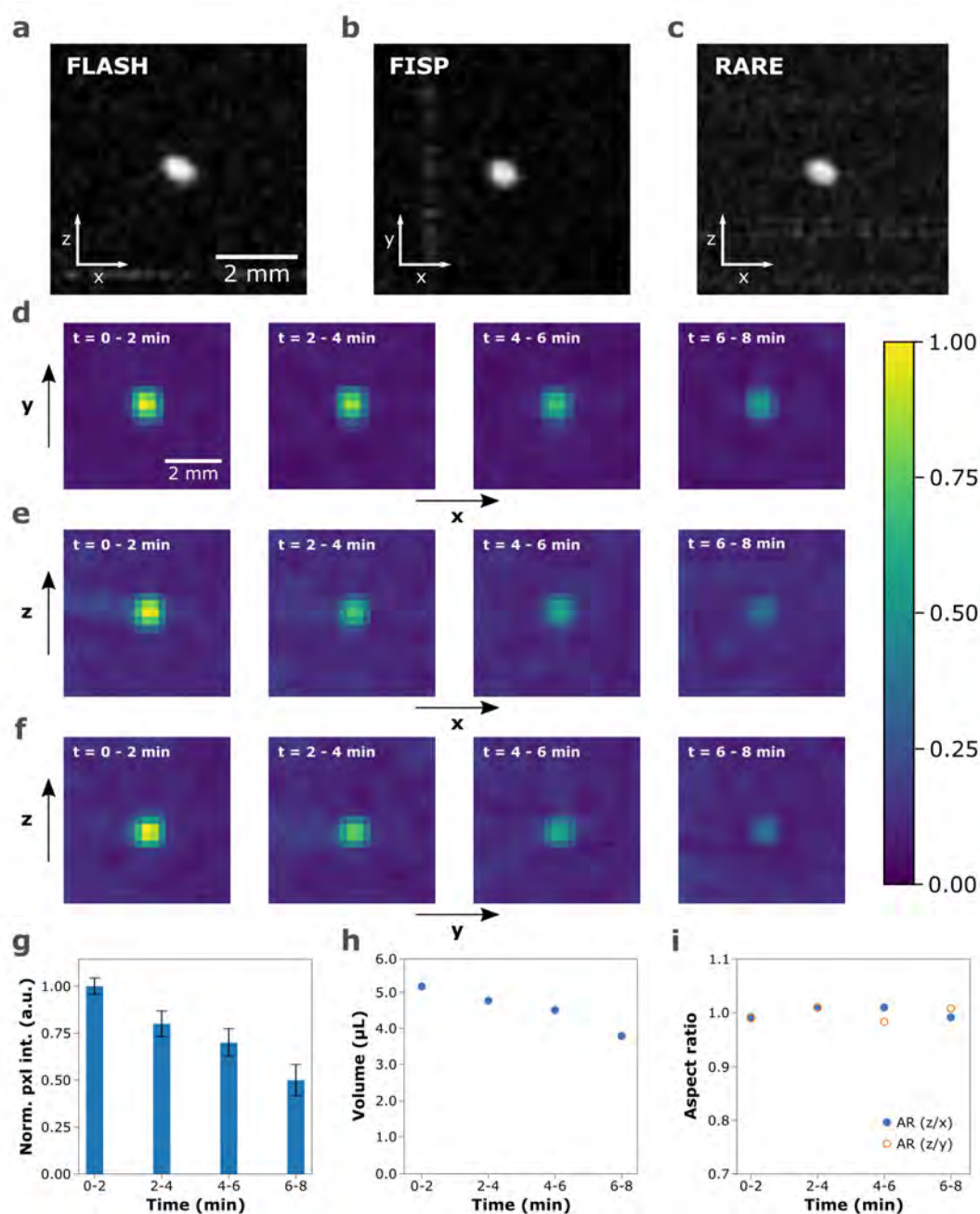
Figure 4.16: MR images of an acoustically levitated droplet of hexadecane acquired with a) FLASH, b) True-FISP, and c) RARE. MR images of an acoustically levitated droplet of water over a period of 8.5 min, were acquired with FLASH along the d) axial (*xy*), e) sagittal (*xz*), and coronal (*yz*) planes. The time in the inset refers to the period of acquisition. g) Average normalized maximum pixel intensity over time. Calculated h) volume, and i) aspect ratio of the water droplet from the FLASH MR images over time.

In Figure 4.16d-f, a levitated droplet of water was visually monitored with the MRI pulse sequence FLASH (fast low angle shot)[72] over a period of 8.5 min. As the evaporation took place, the pixel intensity of the MR images decreased (Figure 4.16g). The volume and aspect ratio of the droplet were determined through image analysis during evaporation. It was found that the pixel intensity and the volume followed the same trend, while the aspect ratio remained close to 1, indicating a spherical droplet. The latter observation was attributed to the low acoustic radiation forces applied on the droplet at 10.0 V inside the magnet.

4.4.2 Magnetic resonance spectroscopy on self-standing droplets

In Figure 4.17a, ^{1}H NMR spectra of levitating canola oil droplets within a defined voxel (localized spectra), and under the whole detection volume of the magnet (non-localized spectra) are shown. From the localized pulse sequences, ISIS (image-selected in viva spectroscopy)[73] led to the highest spectral resolution, in terms of peak intensity and width, as it was shown in the Supporting Information of Paper IV. The non-localized pulse sequences led to equally high spectral resolution, which was comparable, and for certain peaks superior to the spectral resolution acquired with a standard NMR tube, using a standard NMR probe, with the same magnetic field strength.

The chemical shift of the MR spectra acquired on the levitating droplet of canola oil were calibrated by using, as a reference, the spectrum collected with a standard NMR tube. In practice, the shape of the droplet affects the chemical shift, due to changes of the local magnetic field strength in the droplet. In Figure 4.17b, the theoretical chemical shift difference is plotted as a function of the aspect ratio of a hexadecane droplet, as expressed with the equations in the Material and Methods of Paper IV. The more compressed the droplet is, the more pronounced the chemical shift difference from the standard NMR tube was expected to be. In Figure 4.17c, MR spectra of a levitating droplet of hexadecane were acquired at different driving voltages. At low driving voltage, the droplet shape was close to a sphere and as the voltage increased, the droplet became an oblate, since the acoustic pressure applied onto the droplet increased. A downfield shift was observed as the driving voltage increased, which was in line with the theoretical expectations. Following, MR images of the levitating droplet of hexadecane with an in-plane resolution of 625 μm/pxl were

collected with the pulse sequence True-FISP,[74] and the aspect ratio was determined through image analysis. In Figure 4.17d, the theoretical aspect ratio determined from the chemical shift in Figure 4.17c, was compared with the aspect ratio determined through the MR images. In both cases, the aspect ratio followed the same trend, and little variations were found, indicating the possibility of using the chemical shift as a means to determine the shape of the levitating droplet.
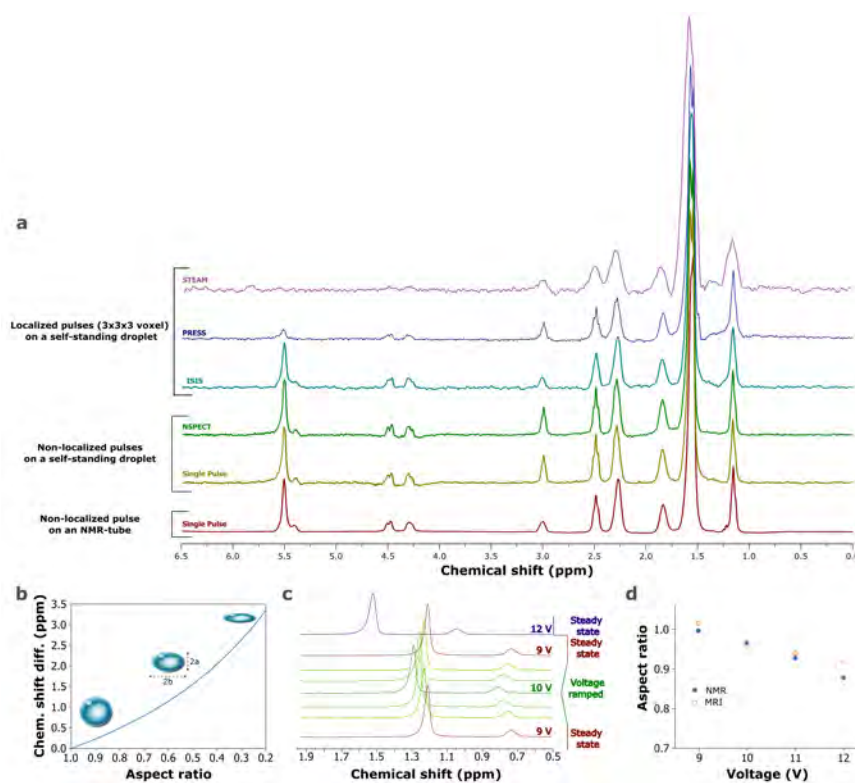

Figure 4.17: a) MR spectra of a canola oil droplet, levitated at 9.0 V, acquired in a 7.05 T magnet with the pulse sequences STEAM, PRESS, ISIS, NSPECT, and Single Pulse, with 66 mm MRI probe, and NMR spectrum of canola oil in a glass tube acquired in a 7.05 T magnet with a 5 mm NMR probe. The chemical shifts of the spectra acquired on the levitated droplet have been shifted to match the spectrum of canola oil in the glass tube. b) Theoretical chemical shift difference for a hexadecane droplet with respect to the aspect ratio, with illustrations of droplets with aspect ratios of 0.9, 0.6, and 0.3, from left to right. c) Representative examples of repeated ISIS MR spectra of an acoustically levitated hexadecane droplet at different voltages (*i.e.*, aspect ratio). d) Aspect ratio of hexadecane droplets determined by combining the MR spectra with the theory presented in the Material and Methods, and aspect ratio determined by MR images of hexadecane levitated at 9 V, 10 V, 11 V, and 12 V.

4.4.3 Molecular interactions within self-standing droplets

Following, the evaporation of a 50 wt% aqueous triethylene glycol (TEG) droplet was chosen to be studied through MR imaging and spectroscopy, due to its high affinity to water, which lead to strong interactions through hydrogen bonding[75]. Figure 4.18a-d presents the MR images and pixel intensity over time. The pixel intensity decreased by approximately 27% within the first 3-6 min of the measurements, due to water evaporation and then remained relatively constant.
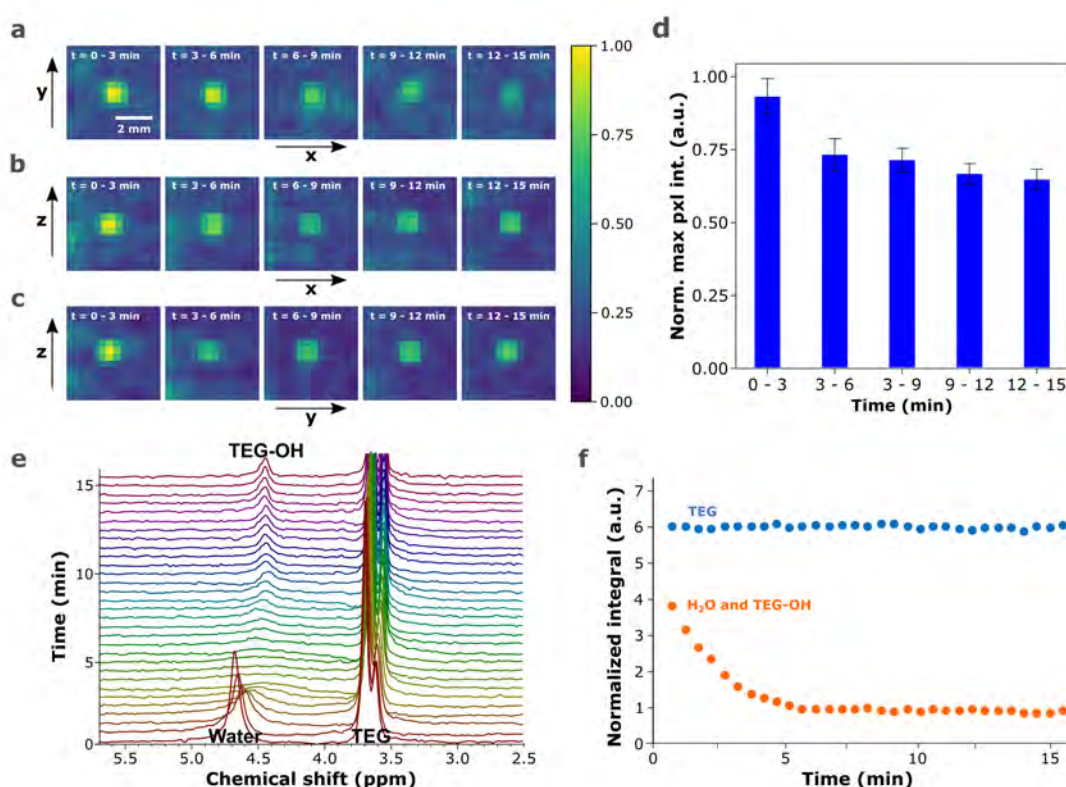
Figure 4.18: FLASH MR images of a 50 wt% TEG aqueous droplet, levitated at 10.0 V along the a) axial (*xy*), b) sagittal (*xz*), and c) corronal *yz* planes, over a period of 15 min, d) normalized maximum pixel intensity with respect to time, e) Time-resolved ISIS MR spectra of a 50 wt% TEG aqueous droplet, levitated at 10.0 V, over a period of approximately 15 min, and f) normalized integrals of MRS signals over time.

In Figure 4.18e, a series of MR spectra, acquired with the localized pulse sequence ISIS, over a period of 16 min is presented. Initially, the -OH signal from the water at 4.7 ppm was high and dominated over the TEG-OH signal in intensity. As evaporation took place, the signal broadened since the solution reached a more equal -OH exchange between water and TEG, due to hydrogen bonding. Finally, the -OH signal from the TEG-OH group appeared at approximately 4.45 ppm, when water evaporated to the extent that the TEG-OH protons were in majority. In Figure 4.18f, the integrals of the NMR signals over the period of 16 min were normalized. The integral from the TEG peaks between 3.4 and 4 ppm remained constant, which was expected as TEG does not evaporate at room temperature; however, the integral from the -OH signals originating from water and TEG-OH decreased and reached a plateau within the first 5 min of the measurements. Furthermore, at the plateau, there is a 6:1 integral ratio between the TEG-OH and TEG, which corresponds to the ratio of hydrogen atoms in the main chain and in the carbons present at the extremities of the TEG molecule. This indicated that the water had fully evaporated.

4.5 Phase transition induced by CO_2 on a single droplet (Paper V)

In Paper V, a pH-responsive system consisting of 2 wt% 12-hydroxystearic acid (HSA) was studied. Choline hydroxide and monoethanolamine (MEA), at different ratios, were used as counter-ions to dissolve HSA. The counter-ion(s) ratio r, is defined as:

$$r = C_{\text{choline}} / (C_{\text{MEA}} + C_{\text{choline}})$$ (4.1)

where C is the concentration.

To induce a pH change, CO_2 was used, allowing to control the kinetics through the gas flow rate. The induced changes were observed through optical observations, X-ray scattering, and magnetic resonance spectroscopy.

4.5.1 Phase diagram of 12-HSA

Initially, the phase diagram of the system (see Figure 4.19) was determined through microscopy observations, pH measurements, small angle neutron scattering (SANS), small angle X-ray scattering (SAXS), and wide angle X-ray scattering (WAXS). It was found that, when only MEA was present as a counter-ion, $r=0.0$, then multi-lamellar tubes were present. As the fraction of choline was increased in the system, more micelles appeared in solution, until only micelles were found, in the case where choline was the only counter-ion, $r=1.0$. When the pH decreased below 8, only multi-lamellar tubes were present, regardless of the counter-ion ratio.
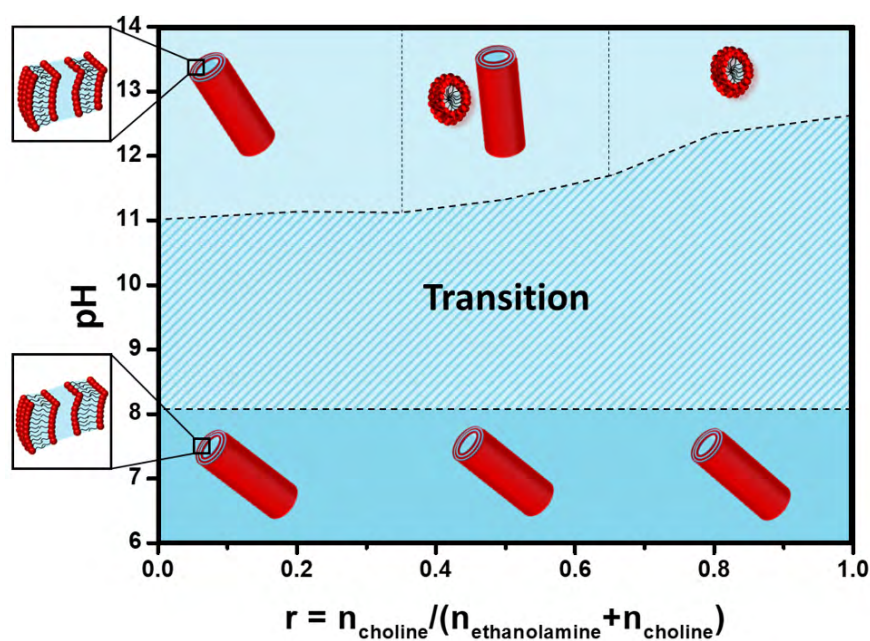

Figure 4.19: Phase diagram of 2 wt% HSA at different counter-ion ratios and pH values. Illustrations of the multi-lamellar tubular structures and the micelles are shown. The area with the dashed lines indicates an intermediate state where both phases are present. Below that area, a clear transition was observed.

4.5.2 Contact-free optical characterization

Microliter droplets of 2 wt% HSA at different counter-ion(s) ratios, containing a universal pH indicator, were levitated and observed through a color camera, while exposed to a flow of CO_2. In Figure 4.20, the color and shape changes of the droplets with counter-ion ratios of $r=0.0$, $r=0.5$, and $r=1.0$, within the first minute of CO_2 exposure, are presented. The droplets with higher counter-ion ratio r, presented a more gradual change in color and a more rapid change in aspect ratio, owing to the lower gelling at the interface, which allowed the CO_2 to interact with the bulk droplet, not only with the interface. As shown in Chapter 2 and previous publications[21,35] the shape of the droplet becomes more compressed when the surface tension decreases, assuming that the volume and acoustic pressure remain constant (Figure 2.1c). In the Supporting Information of Paper V, the acoustic pressure in the presence of CO_2 was simulated, and negligible changes were found. This indicated that the decrease in aspect ratio was due to the decrease of surface tension in the CO_2 environment, which is supported by previous publications[76,77].
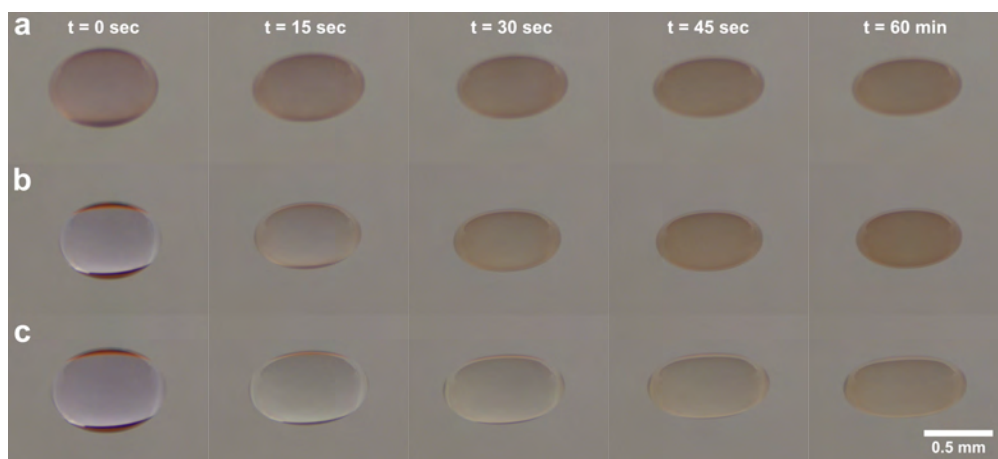

Figure 4.20: Photographs of 2 wt% HSA acoustically levitated droplets exposed to CO2 at time 0, 15, 30, 45, and 60 sec with counter-ion ratios of a) $r = 0.0$, b) $r = 0.5$, and c) $r = 1.0$.

The droplets were acoustically levitated for 15 min in CO_2 flow and from the camera observations, the droplets evaporated less in comparison to the droplets that evaporated in air. This was attributed to the gelling at the interface due to the interactions with

CO_2 which delayed the mass transport of water from the droplet. Specifically, the droplets did not exceed a content of 5 wt% in HSA, while based on microscopy observations of 10 wt% HSA samples, the phase diagram in Figure 4.19, remained unchanged at high pH. Following the 15 min acoustic levitation of the droplets, the samples were collected and observed under the optical microscope, and the presence of multi-lamellar tubes was visible in all samples, indicating that CO_2 did induce a phase transition.

4.5.3 Contact-free structural analysis

The structural changes of the self-assemblies within the levitating droplets, resulting from the exposure to CO_2, were evaluated by combining acoustic levitation with X-ray scattering. Three consecutive measurements were performed within the time frames of 0-5 min, 5-15 min, and 15-25 min, where at time $t=0$ min the CO_2 flow was initiated. In Figure 4.21, the kinetics of the phase transition for the samples with counter-ion ratios of, $r=0.0$, $r=0.5$, and $r=1.0$ are presented. In all cases, a gel Lβ state, and the presence of multi-lamellar tubes, in a triclinic lateral packing of HSA, after 25 min of CO_2 exposure were confirmed[78]. Overall, a shift towards higher q values was observed in all droplets, indicating a decrease in the interlamellar distance inside the tube. This decrease was more prominent as the counter-ion ratio r, increased.
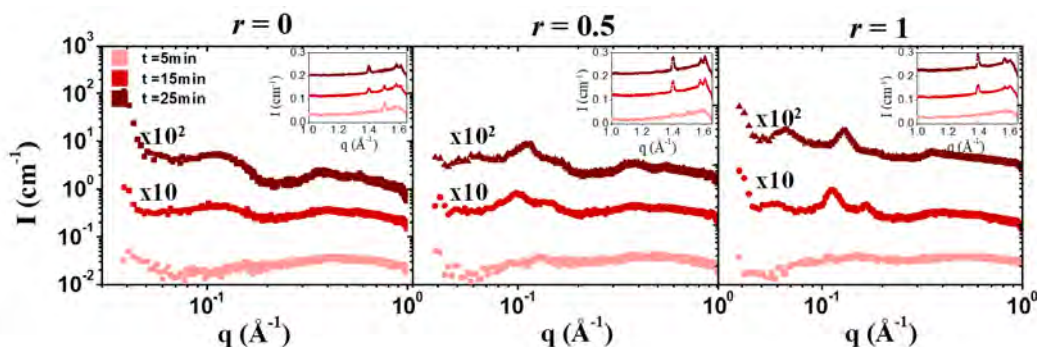

Figure 4.21: SAXS intensity profiles $r = 0.0$, $r = 0.5$, and $r = 1.0$ at $t = 5$ min, $t = 15$ min, and $t = 25$ min of CO_2 exposure. The insert of each spectrum represents the corresponding WAXS diffractograms at $t = 5$ min, $t = 5$ min, and $t = 25$ min of CO_2 exposure. The spectra are shifted in intensity for clarity.

4.5.4 Contact-free magnetic resonance spectroscopy

The mobility of water inside the 2 wt% HSA droplets with r=0.0, r=0.5, and r=1.0 was evaluated by coupling acoustic levitator, Mk3, with a 7.05 T magnet, as described in Paper IV. The droplets were acoustically levitated, and a series of ^{1}H NMR spectra were acquired, in either a CO_2 or air environment. In Figure 4.22a, it can be seen that the linewidth increased more, for lower counter-ion ratios, r, indicating that the molecular motion of the water molecules decreased when a higher amount of MEA was used as a counter-ion. These results were compared with the T_2 spin-spin relaxation times of the samples, measured in standard NMR tubes, and it was found that the T_2 time was higher for lower counter-ion ratio, which was in agreement with the above observations. This was attributed to the higher population of multi-lamellar tubes when a higher concentration of MEA was present as a counter-ion.
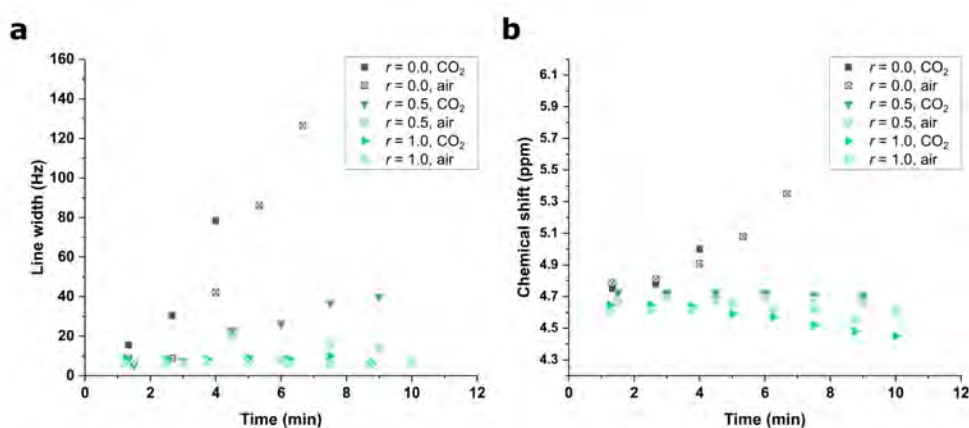

Figure 4.22: a) Linewidth at half maximum height, and b) chemical shift of the water peaks from 1H MR spectra on acoustically levitated droplets with initial content of 2 wt% HSA, and counter-ion ratios of 0, 0.5, and 1, respectively, under CO_2 exposure (filled points) and air (cross-marked points).

Following, the change in chemical shift was examined as a function of time while the droplets evaporated in either a CO_2 or an air environment. This parameter relates to the chemical environment and the shape of the droplets, as shown in Paper IV; however, the ^{1}H NMR measurements performed in the standard NMR tube did not show a change in chemical shift due to the pH change. Consequently, the chemical

shift was mainly attributed to changes in the shape of the droplet. In Figure 4.22b, a downfield shift is observed in the case of $r=0$, while for $r=0.5$, and $r=1.0$, the chemical shift either remained approximately constant, or decreased. Based on the theory developed in Paper IV a compressed droplet, an approximately unchanged droplet and a more spherical droplet would be expected for $r=0$, $r=0.5$, and $r=1.0$, respectively. These changes follow the expected shape changes in aspect ratio observed with the camera when the droplets evaporated in air. However, in the case of CO^2 environment, the situation was not following the expectations. It is important to note that the aspect ratio of the droplet, depends greatly on the volume of the droplet, particularly when low acoustic pressure is applied. In the present case, minor variations in chemical shift could be attributed to limited variations in aspect ratio for these reasons.

5

Conclusions

Acoustic levitation presents numerous possibilities for the study of small-volume samples in a contact-free manner. This thesis underscores the multiple applications of acoustic levitation in the study of soft matter, given the appropriate conditions, in terms of performance and customization, are met.

In Paper I, three customized designs of acoustic levitators (Mk1, Mk2, and Mk3) were theoretically and experimentally evaluated. The transducers of levitators Mk1 and Mk2 were positioned in a circular arrangement, while for Mk3 a hexagonal packing was implemented. Based on the simulations, levitator Mk3 presented the highest acoustic pressure in all dimensional planes (*i.e.*, *xz*, *yz*, and *xy*), while Mk1 and Mk2 exhibited similar levels of acoustic pressure, confirming the dependence between the distance of opposing arrays, and the number of transducers. Furthermore, the frequency response was found to be a good guide for determining the optimum distance between the opposing arrays and fine-tuning the operating frequency of a specific levitator. In terms of experimental performance, the levitator Mk3 presented the highest spatial stability, and levitation capacity, which was in agreement with the simulations. Levitators Mk1 and Mk2 presented similar spatial stability and levitation capacity. However, Mk1 showed higher horizontal stability in comparison to Mk2, potentially due to induced curl forces in the force field of levitator Mk2. Additionally, arranging the transducers in a hexagonal pattern has proven to be beneficial in the performance of the acoustic levitator. The outcome of this study was implemented

into an interactive online framework, which allows the customization of acoustic levitators, for specific applications.

In Paper II, the relationship between droplet shape and surface tension was delved with machine learning. The adequate stability of levitator Mk1 allowed the acquisition of a large dataset of acoustically levitated aqueous surfactant droplets, under various conditions. However, the effect of the acoustic radiation force could not be directly related to the deformation and the surface tension through the existing models. Machine learning was therefore utilized as a tool to determine the underlying correlations between the droplet contours, and the surface tension, without any set preconditions. Droplets from a series of surfactant solutions (SDS, CTAB, and TritonX-100) were acoustically levitated over a period of 30 min, while the voltage was continuously varied, and in total over 50,000 photographs of droplets were collected. The neural network allowed the accurate determination of surface tension throughout the adsorption isotherms of all three surfactants. Moreover, the machine learning algorithm surpassed physical conditions and restrictions that were assigned in previous theoretical models, while the accuracy remained equally high, and in certain cases higher.

In Paper III, acoustic levitator Mk1 was utilized for the study of a binary-droplet system of immiscible liquids. The phenomenon of surface freezing of hexadecane was observed macroscopically up to 3 K above the melting point when the hexadecane droplet was in contact with water. It was found that surface active impurities present in alkanes affected the conditions under which the surface freezing occurred. Another parameter that significantly influenced this effect was the humidity, which affected the evaporation rate of water and consequently the heat transfer between the two levitating droplets. Owning to the high levitation force and stability of levitator Mk3, Raman spectroscopy studies were performed on the droplets. This allowed the investigation of hexadecane in solid phase and the quantified evaluation of the melting kinetics. Overall, this study paves the way for studying binary-droplets systems in a contact-free manner, and the suitability of acoustic levitation as a method for investigating phenomena in environmental and atmospheric sciences.

In Paper IV, magnetic resonance studies were performed on self-standing droplets by developing a demagnetized version of acoustic levitator Mk3. Three different MRI pulse sequences were performed on acoustically levitated droplets, which allowed acquiring of good-quality MR images and following the evolution of evaporation.

Moreover, the relationship between the droplet shape and chemical shift was established from a theoretical and spectroscopy standpoint, owning to a change of magnetic field strength locally. Lastly, dynamic molecular interactions were followed, while quantitative evaluations were performed on microliter droplets.

In Paper V, a pH-responsive system was evaluated in a contact-free manner by flowing CO_2 in close proximity to the levitating droplet. The CO_2 did not affect the stability of the droplet while the system was characterized through optical means, X-ray scattering, and magnetic resonance spectroscopy. By coupling acoustic levitation with the above techniques, the characterization of the sample in terms of pH, surface tension, phase transition, and molecular changes was performed in real-time. This approach allows the direct study of systems in the microliter regime, without compromising the performance of advanced analytical tools, and provides a suitable background for the investigation of complex systems.

These contributions highlight the applicability of acoustic levitation in the study of interfacial and bulk phenomena on self-standing droplets, after proper customization of the device is achieved. Future studies may focus on the adjustment of the individual arrays for the rotational control of a spherical droplet, or positional control of multiple droplets. These developments could lead to the study of droplet collision and mixing of systems, in real-time. Furthermore, increasing the magnetic resonance image resolution of the acoustically levitated droplets, leading to more advanced MRI studies, can also be considered. The possibilities are endless, with our imagination being the only constraint.

Acknowledgements

References

[1] J. R. Moffitt, Y. R. Chemla, S. B. Smith, and C. Bustamante, "Recent advances in optical tweezers," *Annual Review of Biochemistry*, vol. 77, pp. 205–228, 2008.

[2] P. Polimeno, A. Magazzu, M. A. Iati, F. Patti, R. Saija, C. D. E. Boschi, M. G. Donato, P. G. Gucciardi, P. H. Jones, G. Volpe, *et al.*, "Optical tweezers and their applications," *Journal of Quantitative Spectroscopy and Radiative Transfer*, vol. 218, pp. 131–150, 2018.

[3] G. Pesce, P. H. Jones, O. M. Maragò, and G. Volpe, "Optical tweezers: Theory and practice," *The European Physical Journal Plus*, vol. 135, pp. 1–38, 2020.

[4] J. Xie, P. Zhao, C. Zhang, J. Fu, and L.-S. Turng, "Current state of magnetic levitation and its applications in polymers: A review," *Sensors and Actuators B: Chemical*, vol. 333, p. 129533, 2021.

[5] S. Ge, A. Nemiroski, K. A. Mirica, C. R. Mace, J. W. Hennek, A. A. Kumar, and G. M. Whitesides, "Magnetic levitation in chemistry, materials science, and biochemistry," *Angewandte Chemie International Edition*, vol. 59, no. 41, pp. 17810–17855, 2020.

[6] S. R. Dabbagh, M. M. Alseed, M. Saadat, M. Sitti, and S. Tasoglu, "Biomedical applications of magnetic levitation," *Advanced NanoBiomed Research*, vol. 2, no. 3, p. 2100103, 2022.

[7] R. W. Hyers and J. R. Rogers, "A review of electrostatic levitation for materials research," *High Temperature Materials and Processes*, vol. 27, no. 6, pp. 461–474, 2008.

[8] P.-F. Paradis, T. Ishikawa, G.-W. Lee, D. Holland-Moritz, J. Brillo, W.-K. Rhim, and J. T. Okada, "Materials properties measurements and particle beam interactions studies using electrostatic levitation," *Materials Science and Engineering: R: Reports*, vol. 76, pp. 1–53, 2014.

[9] M. P. SanSoucie, "An overview of ground-based electrostatic levitation," *Metallurgy in Space: Recent Results from ISS*, pp. 223–233, 2022.

[10] M. A. Andrade, A. Marzo, and J. C. Adamowski, "Acoustic levitation in mid-air: Recent advances, challenges, and future perspectives," *Applied Physics Letters*, vol. 116, no. 25, 2020.

[11] S. Santesson and S. Nilsson, "Airborne chemistry: Acoustic levitation in chemical analysis," *Analytical and bioanalytical chemistry*, vol. 378, pp. 1704–1709, 2004.

[12] R. J. Weber, C. J. Benmore, S. K. Tumber, A. N. Tailor, C. A. Rey, L. S. Taylor, and S. R. Byrn, "Acoustic levitation: Recent developments and emerging opportunities in biomaterials research," *European Biophysics Journal*, vol. 41, pp. 397–403, 2012.

[13] C. Benmore and J. Weber, "Aerodynamic levitation, supercooled liquids and glass formation," *Advances in Physics: X*, vol. 2, no. 3, pp. 717–736, 2017.

[14] A. Amar, E. Groß-Hardt, A. Khrapitchev, S. Stapf, A. Pfennig, and B. Blümich, "Visualizing flow vortices inside a single levitated drop," *Journal of Magnetic Resonance*, vol. 177, no. 1, pp. 74–85, 2005.

[15] W.-H. Sung, Y.-T. Tsao, C.-J. Shen, C.-Y. Tsai, and C.-M. Cheng, "Small-volume detection: Platform developments for clinically-relevant applications," *Journal of Nanobiotechnology*, vol. 19, no. 1, pp. 1–14, 2021.

[16] Y. Mao, M. Yang, T. Wang, F. Wu, and B. Qian, "Influence of vacuum level on heat transfer characteristics of maglev levitation electromagnet module," *Applied Sciences*, vol. 10, no. 3, p. 1106, 2020.

[17] R. Mondragon, L. Hernandez, J. E. Julia, J. C. Jarque, S. Chiva, B. Zaitone, and C. Tropea, "Study of the drying behavior of high load multiphase droplets in an acoustic levitator at high temperature conditions," *Chemical engineering science*, vol. 66, no. 12, pp. 2734–2744, 2011.

[18] D. Holland-Moritz, B. Nowak, F. Yang, and A. Meyer, "Structure and dynamics of glass-forming alloy melts investigated by application of levitation techniques," *Pure and Applied Chemistry*, vol. 91, no. 6, pp. 895–910, 2019.

[19] C. Chilowsky and P. Langevin, *Production of submarine signals and the location of submarine objects*, US Patent, US1471547A, Oct. 1923.

[20] G. R. Dunlop, "Ultrasonic transmission imaging," PhD dissertation, University of Canterbury, 1978.

[21] Y. Tian, R. G. Holt, and R. E. Apfel, "Deformation and location of an acoustically levitated liquid drop," *The Journal of the Acoustical Society of America*, vol. 93, no. 6, pp. 3096–3104, 1993.

[22] M. A. Andrade, S. Polychronopoulos, G. Memoli, and A. Marzo, "Experimental investigation of the particle oscillation instability in a single-axis acoustic levitator," *AIP Advances*, vol. 9, no. 3, p. 035 020, 2019.

[23] J. Weber, C. Rey, J. Neuefeind, and C. Benmore, "Acoustic levitator for structure measurements on low temperature liquid droplets," *Review of Scientific Instruments*, vol. 80, no. 8, p. 083 904, 2009.

[24] S.-M. Argyri, C. Andersson, N. Paillet, L. Evenäs, J. Ahrens, A. Marzo, V. Contreras, and R. Bordes, "Customized and high-performing acoustic levitators for contact-free experiments," *Journal of Science: Advanced Materials and Devices*, p. 100 720, 2024.

[25] A. Marzo, A. Barnes, and B. W. Drinkwater, "Tinylev: A multi-emitter single-axis acoustic levitator," *Review of Scientific Instruments*, vol. 88, no. 8, p. 085 105, 2017.

[26] A. Marzo, T. Corkett, and B. W. Drinkwater, "Ultraino: An open phased-array system for narrowband airborne ultrasound transmission," *IEEE Transactions on Ultrasonics, Ferroelectrics, and Frequency Control*, vol. 65, no. 1, pp. 102–111, 2017.

[27] L. Cox, A. Croxford, B. Drinkwater, and A. Marzo, "Acoustic lock: Position and orientation trapping of non-spherical sub-wavelength particles in mid-air using a single-axis acoustic levitator," *Applied Physics Letters*, vol. 113, no. 5, p. 054 101, 2018.

[28] T. Omirou, A. Marzo, S. A. Seah, and S. Subramanian, "Levipath: Modular acoustic levitation for 3d path visualisations," in *Proceedings of the 33rd Annual ACM Conference on Human Factors in Computing Systems*, 2015, pp. 309–312.

[29] A. Marzo, S. A. Seah, B. W. Drinkwater, D. R. Sahoo, B. Long, and S. Subramanian, "Holographic acoustic elements for manipulation of levitated objects," *Nature Communications*, vol. 6, no. 1, pp. 1–7, 2015.

[30] A. Marzo and B. W. Drinkwater, "Holographic acoustic tweezers," *Proceedings of the National Academy of Sciences*, vol. 116, no. 1, pp. 84–89, 2019.

[31] A. Watanabe, K. Hasegawa, and Y. Abe, "Contactless fluid manipulation in air: Droplet coalescence and active mixing by acoustic levitation," *Scientific Reports*, vol. 8, no. 1, pp. 1–8, 2018.

[32] M. A. Andrade, F. Buiochi, and J. C. Adamowski, "Finite element analysis and optimization of a single-axis acoustic levitator," *IEEE Transactions on Ultrasonics, Ferroelectrics, and Frequency Control*, vol. 57, no. 2, pp. 469–479, 2010.

[33] V. Contreras and A. Marzo, "Adjusting single-axis acoustic levitators in real time using rainbow schlieren deflectometry," *Review of Scientific Instruments*, vol. 92, no. 1, 2021.

[34] V. Romero-Garcia and A.-C. Hladky-Hennion, *Fundamentals and applications of acoustic metamaterials: from seismic to radio frequency*. John Wiley & Sons, 2019.

[35] W. T. Shi and R. E. Apfel, "Deformation and position of acoustically levitated liquid drops," *The Journal of the Acoustical Society of America*, vol. 99, no. 4, pp. 1977–1984, 1996.

[36] B. O. Enflo and C. M. Hedberg, *Theory of Nonlinear Acoustics in Fluids, Chapter 2 Physical theory of nonlinear acoustics*. Springer, 2002.

[37] C. Andersson and R. Kellnberger, *Levitate: Python implementation of acoustic levitation and related topics*, `https://github.com/AppliedAcousticsChalmers/levitate`, accessed: 2024-03-16, 2021.

[38] A. Arnau, *Piezoelectric transducers and applications*. Springer, 2004.

[39] T. Young, "Iii. an essay on the cohesion of fluids," *Philosophical Transactions of the Royal Society of London*, no. 95, pp. 65–87, 1805.

[40] P.-S. marquis de Laplace, *Supplément à la Théorie de l'action capillaire*. Courcier, 1807.

[41] E. H. Trinh and C.-J. Hsu, "Equilibrium shapes of acoustically levitated drops," *The Journal of the Acoustical Society of America*, vol. 79, no. 5, pp. 1335–1338, 1986.

[42] L. P. Gor'kov, "On the forces acting on a small particle in an acoustical field in an ideal fluid," in *Soviet Physics—Doklady*, vol. 6, 1962, pp. 773–775.

[43] P. L. Marston, "Shape oscillation and static deformation of drops and bubbles driven by modulated radiation stresses—theory," *The Journal of the Acoustical Society of America*, vol. 67, no. 1, pp. 15–26, 1980.

[44] P. L. Marston, S. E. LoPorto–Arione, and G. L. Pullen, "Quadrupole projection of the radiation pressure on a compressible sphere," *The Journal of the Acoustical Society of America*, vol. 69, no. 5, pp. 1499–1501, 1981.

[45] A. N. Kalashnikov and R. E. Challis, "Errors and uncertainties in the measurement of ultrasonic wave attenuation and phase velocity," *IEEE Transactions on Ultrasonics, Ferroelectrics, and Frequency Control*, vol. 52, no. 10, pp. 1754–1768, 2005.

[46] Y. Tian, R. G. Holt, and R. E. Apfel, "A new method for measuring liquid surface tension with acoustic levitation," *Review of Scientific Instruments*, vol. 66, no. 5, pp. 3349–3354, 1995, DOI: 10.1063/1.1145506.

[47] A. Müller, "An X-ray investigation of normal paraffins near their melting points," *Proceedings of the Royal Society of London. Series A, Containing Papers of a Mathematical and Physical Character*, vol. 138, no. 836, pp. 514–530, 1932.

[48] B. Ocko, X. Wu, E. Sirota, S. Sinha, O. Gang, and M. Deutsch, "Surface freezing in chain molecules: Normal alkanes," *Physical Review E*, vol. 55, no. 3, p. 3164, 1997.

[49] X. Wu, B. Ocko, E. Sirota, S. Sinha, M. Deutsch, B. Cao, and M.-W. Kim, "Surface tension measurements of surface freezing in liquid normal alkanes," *Science*, vol. 261, no. 5124, pp. 1018–1021, 1993.

[50] J. P. Janet and H. Kulik, *Machine Learning in Chemistry*. American Chemical Society, 2020.

[51] G. S. Bumbrah and R. M. Sharma, "Raman spectroscopy–basic principle, instrumentation and selected applications for the characterization of drugs of abuse," *Egyptian Journal of Forensic Sciences*, vol. 6, no. 3, pp. 209–215, 2016.

[52] C. V. Raman and K. S. Krishnan, "A new type of secondary radiation," *Nature*, vol. 121, no. 3048, pp. 501–502, 1928.

[53] K. J. Rothschild, I. M. Asher, H. E. Stanley, and E. Anastassakis, "Raman spectroscopy of uncomplexed valinomycin. 2. Nonpolar and polar solution," *Journal of the American Chemical Society*, vol. 99, no. 7, pp. 2032–2039, 1977.

[54] P. A. Bottomley, "Basics of NMR," in *Handbook of Magnetic Resonance Spectroscopy In Vivo: MRS Theory, Practice and Applications*, Wiley, 2016, pp. 26–27.

[55]   R. H. Hashemi, W. G. Bradley, and C. J. Lisanti, *MRI: the basics: The Basics*. Lippincott Williams & Wilkins, 2012.

[56]   T. Narayanan, "Small-angle scattering," *Structure from Diffraction Methods*, pp. 259–324, 2014.

[57]   X. Wang, S. Bashir, and J. L. Liu, *Nanochemistry - From Theory to Application for In-Depth Understanding of Nanomaterials, Chapter 3C.2.1.1 Small- and Wide-Angle Scattering*. De Gruyter, 2023.

[58]   C. Andersson, "Sound field design for transducer array-based acoustic levitation," Ph.D. dissertation, Chalmers Tekniska Högskola (Sweden), 2022.

[59]   O. A. Sapozhnikov and M. R. Bailey, "Radiation force of an arbitrary acoustic beam on an elastic sphere in a fluid," *The Journal of the Acoustical Society of America*, vol. 133, no. 2, pp. 661–676, 2013.

[60]   J. D. Berry, M. J. Neeson, R. R. Dagastine, D. Y. Chan, and R. F. Tabor, "Measurement of surface and interfacial tension using pendant drop tensiometry," *Journal of colloid and interface science*, vol. 454, pp. 226–237, 2015.

[61]   A. Fisher, C. Rudin, and F. Dominici, "All models are wrong, but many are useful: Learning a variable's importance by studying an entire class of prediction models simultaneously.," *Journal of Machine Learning Research*, vol. 20, no. 177, pp. 1–81, 2019.

[62]   C. Andersson and J. Ahrens, "Reducing spiraling in transducer array based acoustic levitation," in *2020 IEEE International Ultrasonics Symposium (IUS)*, IEEE, 2020, pp. 1–4.

[63]   S.-M. Argyri, L. Evenäs, and R. Bordes, "Contact-free measurement of surface tension on single droplet using machine learning and acoustic levitation," *Journal of Colloid and Interface Science*, vol. 640, pp. 637–646, 2023.

[64]   A. Goebel and K. Lunkenheimer, "Interfacial tension of the water/n-alkane interface," *Langmuir*, vol. 13, no. 2, pp. 369–372, 1997.

[65]   C. Farnham, K. Emura, and T. Mizuno, "Evaluation of cooling effects: Outdoor water mist fan," *Building Research & Information*, vol. 43, no. 3, pp. 334–345, 2015.

[66]   R. Tuckermann, S. Bauerecker, and H. Cammenga, "IR-thermography of evaporating acoustically levitated drops," *International Journal of Thermophysics*, vol. 26, pp. 1583–1594, 2005.

[67] E. Wulsten and G. Lee, "Surface temperature of acoustically levitated water microdroplets measured using infra-red thermography," *Chemical Engineering Science*, vol. 63, no. 22, pp. 5420–5424, 2008.

[68] S. Corsetti, T. Rabl, D. McGloin, and J. Kiefer, "Intermediate phases during solid to liquid transitions in long-chain n-alkanes," *Physical Chemistry Chemical Physics*, vol. 19, no. 21, pp. 13 941–13 950, 2017.

[69] D. Cholakova and N. Denkov, "Rotator phases in alkane systems: In bulk, surface layers and micro/nano-confinements," *Advances in colloid and interface science*, vol. 269, pp. 7–42, 2019.

[70] M. Cao and P. Monson, "Solid–fluid and solid–solid phase equilibrium in a model of n-alkane mixtures," *The Journal of chemical physics*, vol. 120, no. 6, pp. 2980–2988, 2004.

[71] S. Iliev, S. Tsibranska, A. Ivanova, S. Tcholakova, and N. Denkov, "Computational assessment of hexadecane freezing by equilibrium atomistic molecular dynamics simulations," *Journal of colloid and interface science*, vol. 638, pp. 743–757, 2023.

[72] D. Matthaei, J. Frahm, A. Haase, and W. Hanicke, "Regional physiological functions depicted by sequences of rapid magnetic resonance images," *The Lancet*, vol. 326, no. 8460, p. 893, 1985.

[73] R. J. Ordidge, A. Connelly, and J. A. Lohman, "Image-selected in vivo spectroscopy (ISIS). A new technique for spatially selective NMR spectroscopy," *Journal of Magnetic Resonance (1969)*, vol. 66, no. 2, pp. 283–294, 1986.

[74] A. Oppelt, R. Graumann, H. Barfuss, H. Fischer, W. Hartl, W. Schajor, *et al.*, "FISP — a new fast MRI sequence," *Electromedica*, vol. 54, no. 1, pp. 15–18, 1986.

[75] R. Olsen, B. Kvamme, and T. Kuznetsova, "Hydrogen bond lifetimes and statistics of aqueous mono-, di-and tri-ethylene glycol," *Journal of American Institute of Chemical Engineers*, vol. 63, no. 5, pp. 1674–1689, 2017.

[76] H. E. Gottlieb, V. Kotlyar, A. Nudelman, *et al.*, "NMR chemical shifts of common laboratory solvents as trace impurities," *Journal of organic chemistry*, vol. 62, no. 21, pp. 7512–7515, 1997.

[77] B. Lv, B. Guo, Z. Zhou, and G. Jing, "Mechanisms of CO2 capture into monoethanolamine solution with different CO2 loading during the absorption/desorption processes," *Environmental science & technology*, vol. 49, no. 17, pp. 10 728–10 735, 2015.

[78] M. Almeida, D. Dudzinski, B. Rousseau, C. Amiel, S. Prévost, F. Cousin, and C. Le Coeur, "Aqueous binary mixtures of stearic acid and its hydroxylated counterpart 12-hydroxystearic acid: Fine tuning of the lamellar/micelle threshold temperature transition and of the micelle shape," *Molecules*, vol. 28, no. 17, p. 6317, 2023.